Downloaded from orbit.dtu.dk on: May 09, 2024

DTU Library

Current understanding of ceria surfaces for CO_2 reduction in SOECs and future prospects – A review

Sala, Elena Marzia; Mazzanti, Nicola; Mogensen, Mogens Bjerg; Chatzichristodoulou, Christodoulos

Published in:
Solid State Ionics

Link to article, DOI:
10.1016/j.ssi.2021.115833

Publication date:
2022

Document Version
Publisher's PDF, also known as Version of record

Link back to DTU Orbit

Citation (APA):
Sala, E. M., Mazzanti, N., Mogensen, M. B., & Chatzichristodoulou, C. (2022). Current understanding of ceria surfaces for CO_2 reduction in SOECs and future prospects – A review. *Solid State Ionics*, *375*, Article 115833. https://doi.org/10.1016/j.ssi.2021.115833

General rights
Copyright and moral rights for the publications made accessible in the public portal are retained by the authors and/or other copyright owners and it is a condition of accessing publications that users recognise and abide by the legal requirements associated with these rights.

- Users may download and print one copy of any publication from the public portal for the purpose of private study or research.
- You may not further distribute the material or use it for any profit-making activity or commercial gain
- You may freely distribute the URL identifying the publication in the public portal

If you believe that this document breaches copyright please contact us providing details, and we will remove access to the work immediately and investigate your claim.

Solid State Ionics 375 (2022) 115833

Contents lists available at ScienceDirect

Solid State Ionics

journal homepage: www.elsevier.com/locate/ssi

Current understanding of ceria surfaces for CO_2 reduction in SOECs and future prospects – A review

Elena Marzia Sala *, Nicola Mazzanti, Mogens Bjerg Mogensen, Christodoulos Chatzichristodoulou *

Department of Energy Conversion and Storage, Technical University of Denmark, Fysikvej, Building 310, DK-2800, Kgs. Lyngby, Denmark

ARTICLE INFO

Keywords:
Electrochemical CO_2 reduction
Ceria surfaces
Doping
Lattice strain
Surface orientation
Carbon deposition

ABSTRACT

Ceria-based materials form a very promising class of electrocatalysts for CO_2 reduction in solid oxide electrolysis cells (SOECs). On the pathway towards the implementation of ceria into technological electrodes on a large scale, an in-depth atomistic understanding of the reaction mechanism over ceria surfaces is crucial in order to optimize its intrinsic electrocatalytic activity. In this review article, we offer a critical discussion of the phenomena governing the electrochemical reduction of CO_2 over ceria surfaces. We focus on the steps that limit the reaction rate and on how these can be accelerated by appropriate tuning of ceria properties and defect chemistry, *via* the introduction of tensile or compressive isotropic strain in the lattice, the promotion of a specific surface orientation and the control of the amount of acceptor or donor dopants incorporated in the fluorite structure. Our review aims to gather and examine the evidence of the role that these levers play in altering the energy landscape of the reaction, along with their influence on the capability of ceria to suppress carbon deposition during cell operation. Ultimately, we identify the areas that need further investigation and propose new lines of work towards the performance optimization of ceria as highly efficient catalyst for CO_2 reduction in SOECs.

1. Introduction

The utilization of fossil fuels for electricity and heat production, and for transport account today for the two biggest shares of anthropogenic CO_2 emissions, with 13.94 and 8.26 Gt of CO_2 emitted in the atmosphere in 2018, respectively [1]. Likewise responsible for a substantial fraction of CO_2 emissions is the chemical industry (1.5 Gt CO_2 in 2018 [2]), which is nowadays the largest industrial energy consumer and relies on fossil fuels as the major feedstock for the production of bulk chemicals. Of the total primary demand for oil and gas in 2017, approximately 14% of oil (13 million barrels per day [mb/d]) and 8% of gas (300 billion cubic meters [bcm]) were destined to the production of petrochemicals and their derivatives [2], through an array of very energy-intensive thermal and/or catalytic processes. More alarmingly, the demand for petrochemicals is expected to rise drastically in the next years: the chemical sector is foreseen to account for over a third of the growth in oil demand projected for 2030 and to consume an additional 56 bcm/y of natural gas by the same year [2].

In light of their catastrophic effect on climate, one of the biggest challenges of our era consists of defossilizing the energy infrastructure and the chemical industry. In this context, electrolysis and co-electrolysis of water/steam and carbon dioxide are considered a cornerstone for the future sustainable energy system, enabling the efficient conversion and long-term storage of electrical energy and the sustainable production of fuels and chemicals from renewable sources [3,4].

High temperature solid oxide electrolysis cells (SOECs) are of particular interest in this respect [3,5–13], as they have significant advantages over the more established and mature low-temperature electrolysis technologies of proton exchange membrane electrolysis cells (PEMEC) and alkaline electrolysis cells (AEC). One of the main advantages of SOECs is their capability to combine high production rates (due to thermal activation) with a high conversion efficiency (low cell voltage). Their high conversion efficiency translates into an exceptionally low electrical energy consumption, with recently demonstrated values on a stack level of ca. 3.1 kWh/Nm^3 H_2 and 3.4 kWh/Nm^3 CO for H_2O and CO_2 electrolysis, respectively [14]. In turn, this low electricity consumption results in a decrease of the levelized cost of product (LCOP), being dominated by the cost of electricity [15]. For SOECs operating at 750–850 °C, electrical efficiencies exceeding 95% are

* Corresponding authors.
E-mail addresses: elmasa@dtu.dk (E.M. Sala), nicma@dtu.dk (N. Mazzanti), momo@dtu.dk (M.B. Mogensen), ccha@dtu.dk (C. Chatzichristodoulou).

https://doi.org/10.1016/j.ssi.2021.115833
Received 15 July 2021; Received in revised form 17 November 2021; Accepted 30 November 2021
Available online 16 December 2021
0167-2738/© 2021 The Authors. Published by Elsevier B.V. This is an open access article under the CC BY license (http://creativecommons.org/licenses/by/4.0/).

reported relative to the lower heating value of hydrogen (LHV) [3], 25–30% higher than the low temperature electrolysis technologies [16]. Furthermore, their high production rate capability favors a reduced capital expenditure, since it scales inversely proportionally to the size of the required electrolysis unit. Besides high efficiency and compactness, SOECs offer also the unique capability of directly producing synthesis gas, consisting of a mixture of H_2 and CO, from co-electrolysis of H_2O and CO_2. Syngas is employed as feedstock for the large-scale production of a wide array of specialty and commodity chemicals, such as ethylene and ethanol, and can be further converted into a broad range of hydrocarbon-based fuels, such as methane, methanol, dimethyl ether, synthetic petrol/diesel, and even kerosene via the Fischer-Tropsch process. SOECs offer the additional advantage of adjusting the CO/H_2 ratio needed for a specific downstream catalytic process simply by varying the CO_2/H_2O feed.

It should be emphasized, though, that SOECs operate with steam and in order to realize these low energy consumption values, steam or waste heat that can be used to raise steam must be freely available. Downstream catalytic conversion of syngas to other hydrocarbons is typically exothermic, thereby offering an excellent match with SOECs [17]. Beneficial heat integration possibilities arise also in connection with biogas [18,19] and biomass [20] utilization. In a recent demonstration, SOECs were employed for the upgrading of biogas to pipeline quality methane [21]. Biogas produced from different environments contains from 30% to 45% of CO_2 [22], which can be co-electrolyzed with steam to produce a CO-rich syngas, avoiding the cost of separating the CO_2 from biogas and converting it instead into a valuable product. Alternatively, SOECs can be coupled with biomass gasification for methane and methanol production, offering the external hydrogen source necessary to compensate the low hydrogen-to-carbon molar ratio of woody biomass [17,23]. Finally, the possibility to operate SOEC plants at variable production rate (with a large dynamic range) and with a sufficiently fast response time can help accommodate the variability of renewable electricity [24], and thus provide large scale grid balancing services [25].

Specifically for CO_2 electroreduction, SOECs have been studied since the 1960s, when the technology was first investigated for CO_2 removal from a spacecraft environment and later to produce O_2 for both manned and unmanned space missions to Mars by leveraging its CO_2-rich atmosphere [26]. These efforts continue at present with MOXIE (Mars Oxygen In-Situ Resource Utilization Experiment), a test model that is aboard the Mars 2020 rover as a prototype to test O_2 production from Martian atmospheric CO_2 [27].

Nowadays, SOECs are the most mature amongst the CO_2 electroreduction technologies, approaching a technology readiness level (TRL) of 9 (*competitive manufacturing in operational environment*) [28] and being already commercially available for CO production with a capacity of 96 Nm^3/h CO [14]. The other two technologies for CO_2 electroreduction that are under intense research and development are low-temperature electrolysis cells, in which CO_2 reduction is carried out at temperatures lower than 100 °C using aqueous or polymer electrolytes, and molten carbonate electrolysis cells (MCECs), operating at intermediate temperatures (400–900 °C), where the electrolyte is a carbonate melt. Low-temperature electrolysis technologies have the capability to directly synthesise chemicals such as ethylene, ethanol and formic acid, which cannot be directly produced in a SOEC. However, they still require very large overpotentials at current densities relevant for commercialization (>200 mA/cm^2) [29], and suffer from poor selectivity generating a plethora of products (at varying ratios depending on catalyst and operating conditions) [30–32], raising doubts on the scalability of this technology, currently lying at a TRL of 4 [33]. MCECs, on the other hand, hold the promise of very high current densities, low overpotentials and faradaic efficiencies (FE) close to 100% [34], with the additional advantage of enduring SO_2-containing CO_2 sources, such as flue gas streams from power stations [35]. However, the high corrosivity of molten carbonates is still the big challenge that MCECs have to face, limiting the stage of industrial development of this technology to a TRL of 5 [33].

Hence, SOECs are the only CO_2 electroreduction technology envisioned for industrial-scale in the next decade, with the potential to alter the landscape of the chemical industry by dissociating the production of chemicals from fossil sources. As a stepping stone towards the application of SOECs for large-scale thermo-catalytic processes (where ca. 10,000–100,000 Nm^3/h of CO or 100–1000 kT CO/y are required), industrial plants for the production of fine chemical precursors (ca. 2000 Nm^3/h of CO or 22 kT CO/y required) are envisioned to be developed and integrated with downstream catalytic processes in the coming 10 years [28]. Alongside, the CO production could also be directed towards decentralized plants operating on-demand, drastically reducing the flammability and toxicity hazards associated with the transportation and storage of CO that the large centralized plants face today [33].

In order to make SOECs commercially viable on a large scale as part of a sustainable energy infrastructure and chemical industry, their lifetime needs to be improved. In fact, one of the main challenges associated with the large-scale commercialization of SOECs lies in preventing cell degradation, which derives from the fuel electrode to a significant portion [36–38]. The state-of-the-art electrocatalyst employed in SOECs fuel electrodes is Ni, typically in the form of a porous cermet (ceramic-metal composite) with yttria-stabilized zirconia (YSZ). Ni-YSZ composite cathodes show excellent activity towards CO_2 reduction [39,40]. However, Ni catalyzes CO disproportionation *via* the Boudouard reaction ($2CO_{(g)} \rightleftharpoons C + CO_{2(g)}$) under SOECs operating conditions, resulting in carbon formation above a threshold CO/CO_2 ratio [41]. The accumulation of carbon on the electrode surface results in Ni dusting, *i.e.* Ni removal from the cathode, leading to the fracture of the porous structure over time. Even if C deposition is limited to a degree that cell fracture is avoided, it causes a partial deactivation of the Ni catalyst, which in turn lowers the cell performance [42].

Carbon deposition can be effectively overcome by limiting operation within safe CO/CO_2 ratios, albeit with the requirement for lower CO_2 conversion and increased gas circulation. Nevertheless, other degradation mechanisms will still lower the electrochemical performance of the Ni-YSZ electrode. The two most substantial ones relate to the poisoning of the electrode surface by impurities such as sulphur [39] (present in the gas feed stream when the CO_2 comes from a biomass process) lowering electrochemical activity, and the agglomeration and depletion of Ni from the electrode/electrolyte interface region [43,44]. The latter results in loss of percolation and associated increase in ohmic losses, as well as in loss of three phase boundary (3PB) length, *i.e.* the line where YSZ, Ni, and gas phase meet, which is where the electrochemical reaction occurs.

All the above-mentioned challenges have been addressed in the last decade with the introduction of doped ceria (CeO_2) as a component of the fuel electrode [45–48]. Ceria plays a beneficial role in different aspects, related to enhancing both electrode performance and stability. Firstly, the mixed ionic electronic conducting (MIEC) nature of ceria, under the reducing conditions of the cathode, extends the reaction zone from a 3PB line to a two phase boundary (2PB) surface between the surface of ceria and the gas phase. Importantly, it has been already demonstrated for the water splitting reaction that the ceria-catalyzed (2PB) reaction area holds the predominant contribution on the overall electrode activity, with only minimal contribution of the metal-catalyzed reaction region (3PB), for 3PB/2PB ratios up to $\sim 4 \times 10^3$ cm^{-1} [49]. Additionally, its improved ionic transport compared to YSZ [50] can help extend the utilization length of the cathode and thus improve performance. Indeed, metal-fluorite cathodes of Ni-CGO (Gd-doped ceria) have shown superior electrochemical performance than Ni-YSZ [51,52]. Finally, the electronic conductivity of ceria can compensate at least to some extent for the Ni depletion, thus reducing/delaying this degradation and improving the electrode stability [53]. In a very recent work from Nenning *et al.* [54], single-phase CGO anodes exhibited some of the lowest polarization resistances ever measured for

technological electrodes in SOFCs (see Fig. 1), showcasing the great potential of CGO as Ni-free high-performing electrode for SOCs.

Ceria has also attracted attention due to its remarkable carbon-deposition suppression capability [55–61]. A recent near ambient pressure X-ray photoelectron spectroscopy (NAP-XPS) study showed that the onset of carbon formation occurs on ceria-containing electrodes at much higher overpotentials than for Ni-YSZ electrodes, significantly beyond the operating window of a commercial SOEC stack [62]. Finally, addition of ceria to the Ni-YSZ cermet [63,64] or the application of Cu-CGO electrodes [65] has been shown to increase the sulphur tolerance of the fuel electrode in fuel cell mode.

Increasing the 2PB area of ceria-based cathodes is an obvious approach for well performing technological electrodes, and can be achieved by nanostructuring of the ceria electrocatalysts [47,49,66–68]. Achieving unprecedented electrochemical performance requires that the intrinsic activity of the ceria surface is also optimized. To achieve this, fundamental studies are necessary in order to obtain an in-depth mechanistic understanding of the elementary processes behind the CO_2 reduction mechanism. Evident levers to tailor the properties of ceria surfaces are: doping, strain, and surface orientation [69]. Understanding the influence of the above parameters requires the use of model-type electrodes with well-defined surface area, composition, and surface orientation. Pulsed laser deposition (PLD) has been the technique of choice in that respect for many studies on the (electro)catalytic and transport properties of doped ceria [49,66,70–78]. PLD enables also fine control of the electrode thickness, ensuring electrodes thin enough as to be surface-reaction limited, rather than bulk diffusion limited [79].

Pure and doped ceria have been extensively applied for many decades now, not only as electrode and electrolyte components in SOCs, but also in a variety of industrial processes [80], ranging from automotive three-way catalysts (TWCs) to biomedical applications [81,82] and organic synthesis [83]. Thus, the physical, mechanical, chemical and electrochemical properties of ceria have been thoroughly studied. Ceria has also been vastly investigated both as catalyst and as non-innocent support in the context of CO_2 valorization processes such as CO_2 methanation and dry-reforming of methane, offering an extensive literature covering the interaction of the CO_2 molecule with ceria surfaces in heterogeneous catalysis. A comprehensive and in-depth description of ceria structure, defect chemistry and transport properties [69,81,84–92], as well as an overview of the knowledge gained from its application in CO_2 conversion catalysis [93,94], can be found elsewhere and are beyond the scope of this review. The aim of this review is rather to outline the accomplishments realized up to date in the understanding of the CO_2 reduction pathway over ceria surfaces, along with the challenges and the remaining questions to be answered for the development of better performing ceria-based electrocatalysts for CO_2 reduction in SOECs.

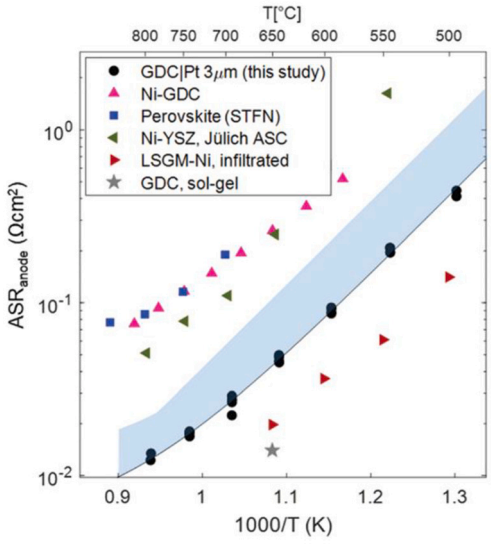

Fig. 1. Arrhenius plot of the polarization resistance of different anode materials combinations used in high power density SOFCs. Reproduced from ref. [54] with permission from the Royal Society of Chemistry.

2. Role of ceria defect chemistry and surface species in the CO_2 electroreduction pathway

The electrochemical reduction of CO_2 to CO is expressed, using Kröger-Vink notation [95], as:

$$CO_{2(g)} + V_O^{\bullet\bullet} + 2e' \rightleftarrows CO_{(g)} + O_O^x \quad (1)$$

where $V_O^{\bullet\bullet}$ denotes a doubly positive charged oxide ion vacancy, and O_O^x a lattice oxygen. In the case of ceria, electrons are localized around Ce ions as small polarons [96], and Eq. (1) can be expressed as follows:

$$CO_{2(g)} + V_O^{\bullet\bullet} + 2Ce_{Ce}^{'} \rightleftarrows CO_{(g)} + O_O^x + 2Ce_{Ce}^x \quad (2)$$

where Ce_{Ce}' represents the Ce^{3+} cations (or localized electrons) and Ce_{Ce}^x the Ce^{4+} cations.

Chueh and co-workers [74] used NAP-XPS to analyze the CO_2 reduction reaction pathway on 20 at.% Sm-doped ceria (SDC) using a model electrochemical cell operating at conditions approximating technologically-relevant ones for SOECs. The authors split the overall reaction into 3 conceptual steps, consisting of the transport of charge carriers from the bulk to the surface, the adsorption/dissociation of the gaseous reactants and the charge transfer at the surface/gas interface. The reaction starts with the migration of polarons (Eq. 3) and oxygen vacancies (Eq. 4) from the bulk of ceria towards its surface. The subscripts "b" and "s" in the following equations refer to bulk and surface species, respectively.

$$2\left(Ce_{Ce,b}^{'} + Ce_{Ce,s}^x \rightleftarrows Ce_{Ce,s}^{'} + Ce_{Ce,b}^x\right) \quad (3)$$

$$V_{O,b}^{\bullet\bullet} + O_{O,s}^x \rightleftarrows V_{O,s}^{\bullet\bullet} + O_{O,b}^x \quad (4)$$

Subsequently, the surface reaction has been represented via two single-electron transfer steps for the two electrons transferred from the ceria surface to the reaction intermediate (in contrast to water splitting, where only one electron is transferred to the hydroxyl ion, $OH_{O,s}^{\bullet}$, upon incorporation of the oxygen ion in an oxygen vacancy [73,97–101]). The first step consists in the activation of a physisorbed CO_2 molecule on a surface oxygen site by a localized electron (Ce^{3+}) (Eq. 5). The C atom of the CO_2 molecule forms a chemical bond with the surface oxygen ion, generating a nonpolar [102] carbonate, $(CO_3)_{O,s}^{'}$, whose configuration and preferential adsorption site are discussed in Section 2.1.

$$CO_{2(g)} + Ce_{Ce,s}^{'} + O_{O,s}^x \rightleftarrows (CO_3)_{O,s}^{'} + Ce_{Ce,s}^x \quad (5)$$

The second step consists of the second electron transfer and oxygen ion incorporation in an oxygen vacancy. The carbonate is decomposed and produces an adsorbed CO, which eventually desorbs from the ceria surface as gaseous product (Eq. 6).

$$(CO_3)_{O,s}^{'} + Ce_{Ce,s}^{'} + V_{O,s}^{\bullet\bullet} \rightleftarrows CO_{(g)} + Ce_{Ce,s}^x + 2O_{O,s}^x \quad (6)$$

A schematic representation of the reaction pathway as described above is proposed in (Fig. 2a).

With respect to the rate limiting steps of the process, some considerations need to be made depending on the system geometry and configuration. In the case of thin film studies, in which the current collection is optimized (to achieve homogeneous current distribution on the entire electrode surface, *e.g.* by sufficiently small mesh spacing of micro-patterned metal grids [103,104]), the charge transport reactions (Eq. 3–4) do not constitute the rate-limiting steps to the overall reaction.

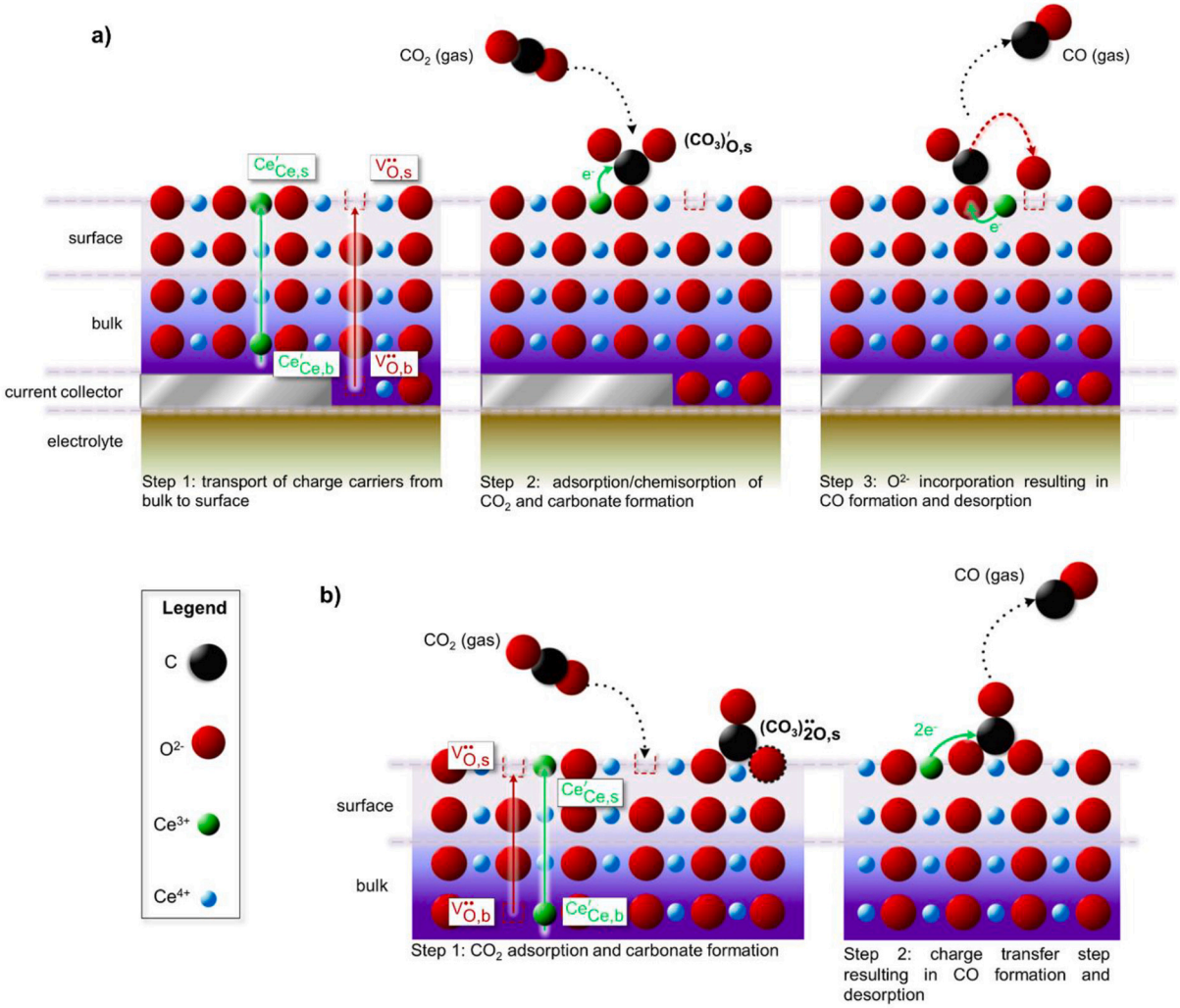

Fig. 2. Schematic representation of the reaction mechanism for a) the CO_2 electroreduction on 20 at.% Sm doped ceria proposed by Chueh and coworkers [74], b) the CO_2 splitting pathway on ceria nanopowders proposed by Zhao *et al.* [106]. In Fig. 2b), two electrons appear to derive from the same Ce ion for the sake of drawing clarity, although in reality two Ce ions are expected to be involved.

This has been demonstrated experimentally for this type of model electrodes both by electrochemical impedance spectroscopy (EIS) [49] and by NAP-XPS [73] in the case of the water splitting reaction. Furthermore, by employing a counter electrode (CE) with substantially higher surface area than the working electrode (WE), it can be assumed that the overpotential at the WE-gas interface dominates the electrode response, with negligible overpotential at the CE. Thus, the surface reaction (Eq. 5–6) can be probed under polarization as the one kinetically limiting the entire process [74].

In order to identify the rate-determining amongst the two single-electron transfer steps, Chueh and co-workers [74] analyzed the correlation between the concentration of near surface Ce^{3+}, denoted hereafter as $[Ce^{3+}{}_s]$, the carbonate coverage and the cathodic overpotential. By increasing the cathodic polarization, the ratio of $[Ce^{3+}{}_s]/([Ce^{3+}{}_s] + [Ce^{4+}{}_s])$ grows linearly up to a value of 45% at the highest measured overpotential of −0.35 V, reflecting a strong degree of reduction at the electrode surface. On the other hand, the carbonate coverage only increases slightly with increasing cathodic polarization and approaches saturation at an overpotential of −0.1 V, at a value of approximately 20% of a monolayer. The authors suggest that as the coverage increases, the adsorption enthalpy is expected to rise due to adsorbate–adsorbate interactions, as already suggested by DFT calculations for CO_2 adsorption over CeO_2 surfaces [105]. The fact that the same phenomenon of saturation of the hydroxyl coverage was not observed experimentally for water splitting [73] is attributed to the larger molecular dimensions of carbonates with respect to the hydroxyl ions [74].

Turning to Eq. 5, one can observe that from one hand, the increasing cathodic overpotential translates into an increase of the chemical potential of the localized electrons, driving the reaction towards the forward direction. On the other hand, as soon as the coverage increases above the critical value for which the adsorbate-adsorbate interactions become prominent, there is an increase of the adsorbate's chemical potential, which opposes the charge transfer from the localized electron. According to this reasoning, for large carbonate coverages at sufficiently high overpotential, the first electron transfer could become rate-limiting.

The correlation between $[Ce^{3+}{}_s]$ and carbonate coverage has also been derived and discussed by Zhao *et al.* [106] for CO_2 splitting on highly oxygen-deficient $CeO_{2-\delta}$ and $Ce_{0.5}Zr_{0.5}O_{2-\delta}$ (CZO) nanopowders, reduced by H_2 dosing prior to introduction of CO_2. The experimental design, promoting a surface-limited process, and the kinetic model employed to describe the reaction steps enable a comparison with the study of Chueh and co-workers [74], in which the ion-incorporation flux is controlled by the electrode overpotential. Zhao *et al.* [106] derived a "linear-flattened-decay pattern" for the concentration of carbonate with respect to $[Ce^{3+}{}_s]$. They estimated a maximum value of 10–30% for the carbonate coverage at 500 °C, in line with the 20% deduced in ref. [74] at the same temperature. According to the analysis of Zhao *et al.* [106]

though, the carbonate coverage decreases with increasing degree of surface reduction, instead of reaching the saturation value (plateau) proposed by Chueh and co-workers [74].

The explanation given by Zhao *et al.* [106] is based on the different reaction rates of the adsorption/activation of CO_2 and the charge transfer/desorption of CO. More specifically, they model the mechanism of CO_2 splitting on the ceria surface as comprised of two steps, reported hereafter in Eq. 7 and 8, and illustrated in Fig. 2b:

$$CO_{2(g)} + V^{\bullet\bullet}_{O,s} + O^{x}_{O,s} \rightleftarrows (CO_3)^{\bullet\bullet}_{2O,s} \quad (7)$$

$$(CO_3)^{\bullet\bullet}_{2O,s} + 2Ce'_{Ce,s} \rightleftarrows CO_{(g)} + 2Ce^{x}_{Ce,s} + 2O^{x}_{O,s} \quad (8)$$

Based on their kinetic model fitting results, the CO_2 activation (Eq. 7) is deemed to be energetically favored and exothermic, whereas the charge transfer (Eq. 8) is endothermic and limiting the process, as shown in the energy diagram of Fig. 3. When the $[Ce^{3+}{}_s]$ is low, the charge transfer is slow, so that the carbonate concentration is only controlled by the CO_2 activation, giving a linear increase of adsorbates with $[Ce^{3+}{}_s]$ due to the associated increase in the concentration of $V_{O,s}^{\bullet\bullet}$. When the surface is strongly reduced, the charge transfer reaction is sufficiently fast that the accumulation of carbonates resulting from CO_2 activation is slowed down. When the $[Ce^{3+}{}_s]$ increases above ~50–60% (for CeO_{2-x}), the charge transfer reaction becomes faster than Eq. 7 and the carbonate concentration decreases with further increase in $[Ce^{3+}{}_s]$.

A similar increasing-flattened-decay trend of carbonate coverage with cathodic polarization was also observed in one more study employing model electrodes to study the CO_2 electroreduction mechanism *operando* on ceramic electrodes [107]. In this case, the focus was on the perovskites $La_{0.6}Sr_{0.4}FeO_{3-\delta}$ (LSF) and $La_{0.7}Sr_{0.2}Cr_{0.9}Ni_{0.1}O_{3-\delta}$ (LSCrNi), materials closely related to ceria within the broader family of MIEC. Given the similarities to ceria in terms of transport properties and point defects, it is worthwhile highlighting some of the findings obtained for perovskite materials that offer a valuable perspective on how to interpret the data available for ceria. Here, the reaction pathway is divided into 3 steps, described hereafter in Eqs. 9–11 and schematically represented in Fig. 4.

$$CO_{2(g)} + V^{\bullet\bullet}_{O,s} + e' \rightleftarrows (CO_2)^{\bullet}_{O,s} \quad (9)$$

$$(CO_2)^{\bullet}_{O,s} + O^{x}_{O,s} \rightleftarrows (CO_3)^{\bullet}_{2O,s} \quad (10)$$

$$(CO_3)^{\bullet}_{2O,s} + e' \rightleftarrows CO_{(g)} + 2O^{x}_{O,s} \quad (11)$$

According to Opitz *et al.* [107], two pathways are possible for the first step of CO_2 adsorption and carbonate radical formation (Eq. 9): in one case, the CO_2 adsorption and first electron transfer occur as one single step upon adsorption into a singly charged oxygen vacancy, *i.e.* an oxygen vacancy in which an electron is trapped; in the other, the CO_2 molecule is firstly adsorbed on an oxygen vacancy, followed by the charge transfer from a polaron or the conduction band. For the sake of simplicity, only the first pathway is depicted in Fig. 4.

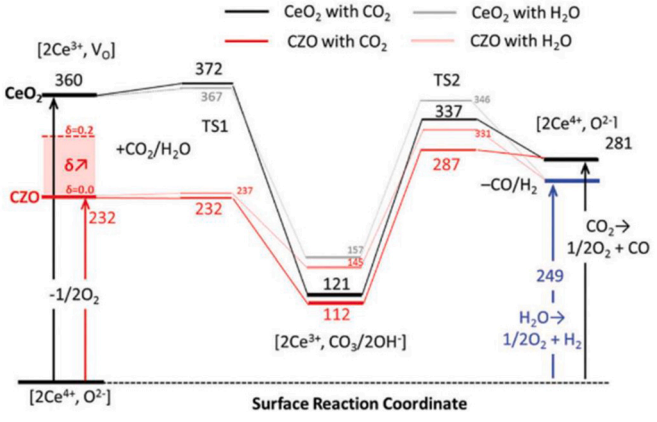

Fig. 3. Energy landscape (unit: kJ/mol) for the CO_2 reduction and H_2O splitting pathways over ceria (black lines) and CZO (red lines) surfaces proposed by Zhao *et al.* [106]. Reproduced from ref. [106] with permission from the Royal Society of Chemistry. (For interpretation of the references to colour in this figure legend, the reader is referred to the web version of this article.)

Turning to the correlation between carbonate intensity and applied overpotential, in this study the carbonate coverage saturation or maximum is shifted to much stronger polarization than the −0.1 V observed for ceria-based electrodes, *i.e.* approx. −0.5 V and − 1.1 V for LSCrNi and LSF, respectively. However, it must be noted that in ref. [107] solely CO_2 is used as feed gas, rather than a mixture of CO/CO_2 as in the study of Chueh and co-workers [74]. Considering as a reference the chemical potential of 1 bar of oxygen, the corresponding calculated oxygen chemical potentials are approximately −2.37 eV for SDC at −0.1 V and 500 °C, −3.15 and − 1.95 eV for LSCrNi at −1.1 V and LSF at −0.5 V at 720 °C, respectively. The corresponding equivalent oxygen partial pressures under these values of cathodic polarization are calculated as $1.2{\cdot}10^{-30}$, $1.6{\cdot}10^{-32}$ and $2.1{\cdot}10^{-20}$ atm for SDC, LSCrNi and LSF, respectively.

Opitz *et al.* [107] observe that the polarization dependence of the carbonate coverage cannot be associated solely with the concentration of oxygen vacancies, as there is negligible carbonate coverage at small-intermediate polarizations despite the fact that the introduction of the acceptor dopants in the analyzed compositions is already compensated by oxygen vacancies to a large extent. The observed behavior suggests that oxygen vacancies are the preferred adsorption site but that electrons are also necessary for the adsorption of CO_2 on perovskites. Firstly, the observation of the carbonate coverage increase with increasing overpotential above a threshold value (despite the presence of surface oxygen vacancies already at zero polarization) suggests that an electron transfer is indeed necessary for the formation of the carbonate intermediate. Secondly, the presence of a saturation limit or maximum seems to indicate that the rate-limiting step is the one following the carbonate formation, *i.e.* the reduction of the carbonate to CO. Thirdly, the correlation of the saturation limit or maximum in carbonate coverage with acceptor doping (and associated oxygen vacancy concentration) suggests oxygen vacancies as the preferred adsorption site. Finally, the depletion of the carbonate at even stronger cathodic polarizations suggests that this rate-limiting step is also accelerated by the overpotential.

The authors point out that this overpotential dependence of the rate-limiting step is consistent with the exponential polarization dependence of the electron concentration in MIECs, resulting in the exponential current−overpotential characteristics observed for all four perovskite compositions investigated (Fig. 5a). This exponential behavior cannot be attributed to a Butler-Volmer type electron transfer over an activation barrier since the carbonate intermediate is pinned to the Fermi level of the perovskite surface, as the −1 eV/V shift of the binding energy of the carbonate intermediate vs. polarization suggests. An exponential trend is also found for the current density as a function of the applied overpotential by Chueh and co-workers [74] for 20 at.% Sm-doped ceria (Fig. 5b), and for the ion incorporation flux as a function of the $[Ce^{3+}{}_s]$ in $Ce_{0.5}Zr_{0.5}O_{2-\delta}$ by Zhao *et al.* [106]. The −1 eV/V shift of the binding energy of the carbonate intermediate vs. polarization, observed by Skafte *et al.* [62] for 20 at.% Sm-doped ceria, suggests again that it is the abundance of $[Ce^{3+}{}_s]$ that controls the rate of the second electron transfer step in Eq. 6 or Eq. 8.

Another interesting inference can be drawn from this study in association with the observed correlation of the carbonate intensity with the level of acceptor doping for the different compositions examined. The carbonate intensity started increasing at less reducing potential with increasing acceptor doping and reached a higher value at its maximum. This suggests that adsorbate-adsorbate interactions are not the sole factor potentially limiting carbonate coverage, at least for these perovskite compositions.

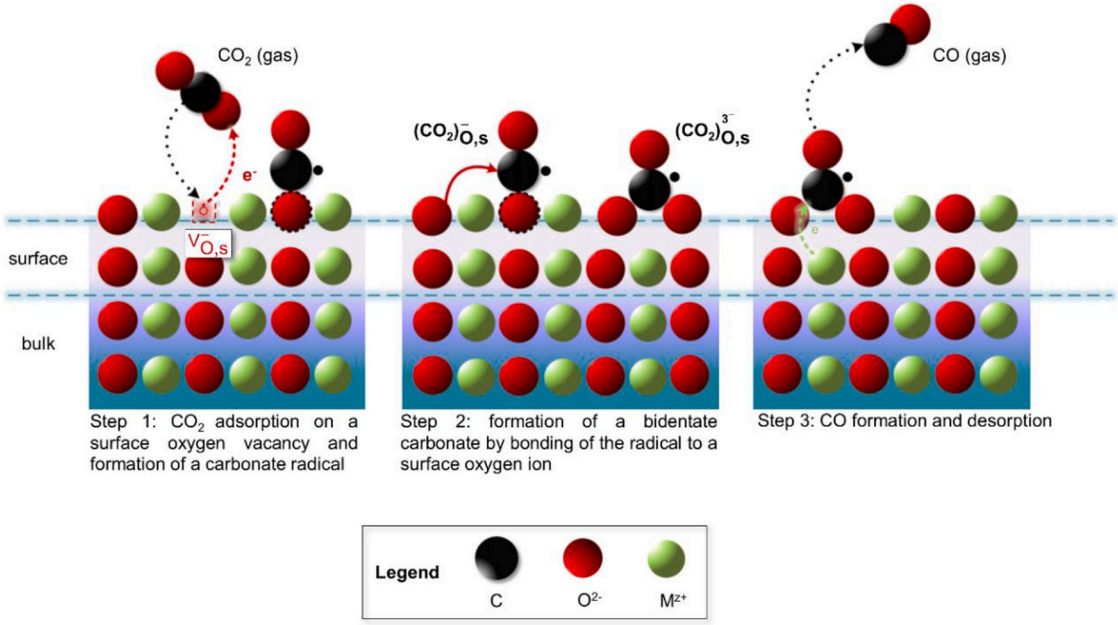

Fig. 4. Schematic representation of the CO_2 electroreduction pathway on a perovskite structure as proposed by Opitz *et al.* [107].

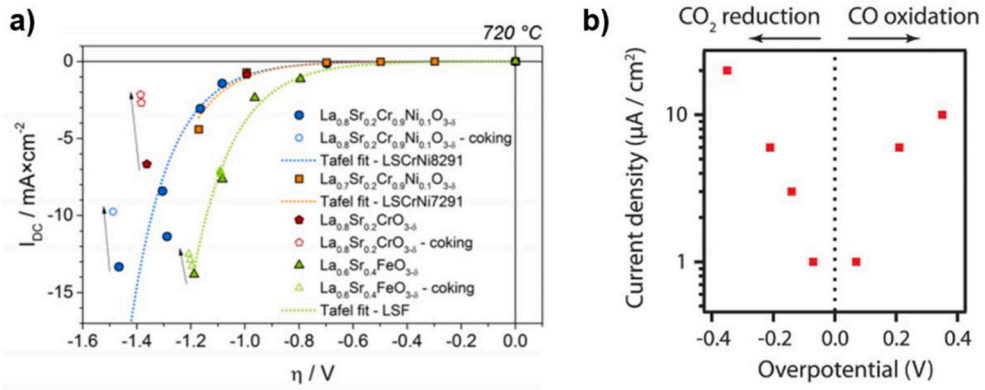

Fig. 5. Current−voltage characteristics of: a) the four different composition of perovskite model electrodes investigated by Opitz *et al.* [107]. Measurements were made at 720 °C in 0.25 mbar CO_2 Reprinted with permission from *ACS Appl. Mater. Interfaces* 2017, 9, 41, 35,847–35,860 [107]. Copyright © 2017 American Chemical Society. b) the 20 at.% Sm-doped ceria model electrode investigate by Chueh and co-workers [74] at 500 °C in a 270 mTorr CO/CO_2 mixture. Reproduced from ref. [74] with permission from the Royal Society of Chemistry.

Ultimately, one can conclude that some similarities exist in the behavior of the two families of oxides. Firstly, the crucial role of surface oxygen vacancies and electrons needed for the CO_2 chemisorption and carbonate formation emerges. Secondly, in both systems there appears to be a second electron transfer step which is accelerated with increasing polarization (and associated electron concentration), shifting the balance towards the CO_2 chemisorption becoming the rate limiting step at high polarizations. However, further electrochemical studies on model electrodes are necessary in order to unequivocally elucidate the nature of the correlation between [$Ce^{3+}{}_s$] and carbonates in ceria, particularly in conditions relevant for technologic applications. Firstly, an extension of the NAP-XPS direct spectroscopic determination of carbonate coverage at larger (more negative) polarizations than those covered by Chueh and co-workers [74] is needed to determine if a maximum is indeed reached in ceria, followed by a decrease with further increase of $Ce^{3+}{}_s$. Keeping in mind that higher overpotentials at low operating temperatures may coincide with the onset of carbon formation (approx. -0.3 V at 550 °C in a mixture of 50/50 CO/CO_2 [62], as explained more in detail in Section 2.4), higher temperatures would probably be more suitable for the purpose. An extension to higher temperatures would also be interesting to determine the trend of carbonate concentration with temperature: the kinetic model developed by Zhao *et al.* [106], indeed, predict that the coverage of carbonate is reversely dependent with temperature for both doped and undoped ceria, *i.e.* a higher carbonate concentration is found at lower temperature. At the very low surface carbonate coverage expected from the calculations (~3% at 700 °C and ~ 0.03% at 900 °C for ceria) the adsorbate-adsorbate interactions will be less prominent, and their role vs. the role of [$Ce_{Ce,\,s}{}^{3+}$] on the relative rate of the different charge transfer steps may be clarified. Finally, the spectroscopic investigation of ceria with different concentration of dopants, inducing different [$V_{O,\,s}{}^{\bullet\bullet}$]/[$Ce_{Ce,\,s}{}^{3+}$] ratios at the surface, would allow to conclude on the importance of oxygen vacancies and/or [$Ce_{Ce,\,s}{}^{3+}$] for the CO_2 adsorption step.

The polarization affects the absolute and relative rates through influencing the surface vacancy and polaron concentration. This can also be adjusted to some extent through surface termination, doping, and strain, such as to accelerate both steps and in particular step *3)* which is rate limiting at low overpotentials (of ca. -0.1 V where technological SOECs typically operate).

2.1. *Influence of low-index surface orientations on the electrochemical activity of ceria towards CO_2 reduction*

The three low-index orientations of CeO_2, i.e. (100), (110), and (111), differ by the number of coordination vacancies around the

KEY POINTS on the pathway of CO_2 reduction on ceria surfaces in SOECs:

- The overall reaction can be divided into 3 conceptual steps, consisting of the *1)* transport of charge carriers from the bulk to the surface, *2)* the adsorption/chemisorption of CO_2 and *3)* the oxygen ion incorporation resulting in CO formation and desorption.
- Steps *2)* and *3)* constitute the surface reaction, in which two electrons are transferred from the ceria surface to a physisorbed CO_2 molecule.
- Under SOEC conditions, the reaction intermediate is a carbonate, CO_3^{2-}, in which the C atom forms a chemical bond with 1–3 surface oxygen atoms (further discussed in Section 2.1). A saturation of the carbonate coverage has been observed with increasing cathodic polarization, attributed to adsorbate-adsorbate interactions or increase in the relative rate of step *3)*/step *2)*. The carbonate coverage should pass through a maximum with overpotential according to the later explanation, offering a clear distinction from the adsorbate-adsorbate interaction hypothesis that future spectroscopic investigations could address.
- There is consensus that the rate limiting step gradually shifts from step *3)* to step *2)* with increasing cathodic polarization.

exposed Ce cations and O anions, their surface site density and interionic distance [87]. Tasker first classified ionic crystal surfaces into three types [108], *i.e.* "type 1, neutral surfaces with stoichiometric proportions of anions and cations in each plane; type 2, charged surfaces, with no dipole moment in the repeat unit perpendicular to the surface; and type 3, charged surfaces that have a dipole moment in the repeat unit perpendicular to the surface". CeO_2 (110) is a type 1 surface, with each layer having zero charge. CeO_2 (111) is a type 2 surface, having every plane charged but a repeating unit consisting of three planes in a symmetrical sequence (exposed oxygen plane above a plane of cerium ions, in turn above an oxygen plane), so that there is no net dipole moment perpendicular to the surface. CeO_2 (100) is a type 3 surface, with alternatingly charged planes and a repeating unit of two planes, which results in a dipole moment perpendicular to the surface. This last type of surfaces have nearly infinite surface energy, with an electric field due to the charged surface, so that they can only exist upon reconstruction of the bulk truncation [87,109–112]. There is broad consensus that the stability of these three surfaces is ranked as (111) > (110) > (100) [113–116], *i.e.* the (100) being the least stable. However, the stability of the surfaces does not reflect the trend of their oxygen vacancy formation energy (reducibility). It is well established through DFT calculations, that less energy is required to form an oxygen vacancy on the (110) surface, compared to the (100) and lastly the (111) [117–121]. It is worthwhile mentioning though that a recent X-ray absorption near-edge structure (XANES) spectroscopy study employing ceria thin films with (100), (110), and (111) terminations showed that the surface concentration of Ce^{3+} (and inferred oxygen vacancy concentration) is equivalent on the three facets under the high temperature and low oxygen partial pressure conditions typical of SOEC [122]. A schematic representation of the three low-index surface terminations of ceria is depicted in Fig. 6. Characteristic properties of each termination and interionic distances are reported in Table 1 and 2, respectively.

The surface orientation, alongside with other parameters such as the active site, the dopant concentration, the degree of coverage and, ultimately, the reaction conditions, is well known for playing a role in the configuration of the adsorbates and reaction intermediates. For ceria surface, the configuration of the carbonate on its three low-index surface orientations is not well established, and sometimes contradicting findings are reported. Various experimental studies employing Fourier transform infrared spectroscopy (FTIR) on ceria and doped-ceria as catalyst [128–132] have shown that the carbonate can have different configurations, *i.e.* mono-, bi- and poly-dentate or bridged, whose structures can be visualized in Fig. 7. Albrecht *et al.* [133] revealed both experimentally and computationally that CO_2 adsorbs as a flat-lying tridentate carbonate both on the oxidized and reduced CeO_2 (100) surfaces. DFT calculations from Cheng *et al.* [134] showed that on the reduced CeO_{2-x} (110) surface the carbonate adsorbs either as mono/bidentate carbonate or bridged, depending on whether the oxygen vacancy site is an in-plane vacancy or a split vacancy (*i.e.* an oxygen vacancy where one of the nearest oxygen anions moves towards the vacancy, occupying a bridge site equidistant to the two adjacent cerium cations), respectively. Finally, on the fully oxidized CeO_2 (111) surface the carbonate adsorbs as a monodentate up to a coverage of 1/3 monolayer (ML), whereas for higher coverages mixed configurations (monodentate + linear in two different partial layers) are present [105,135]. DFT calculations from Skafte *et al.* [62] confirm the above

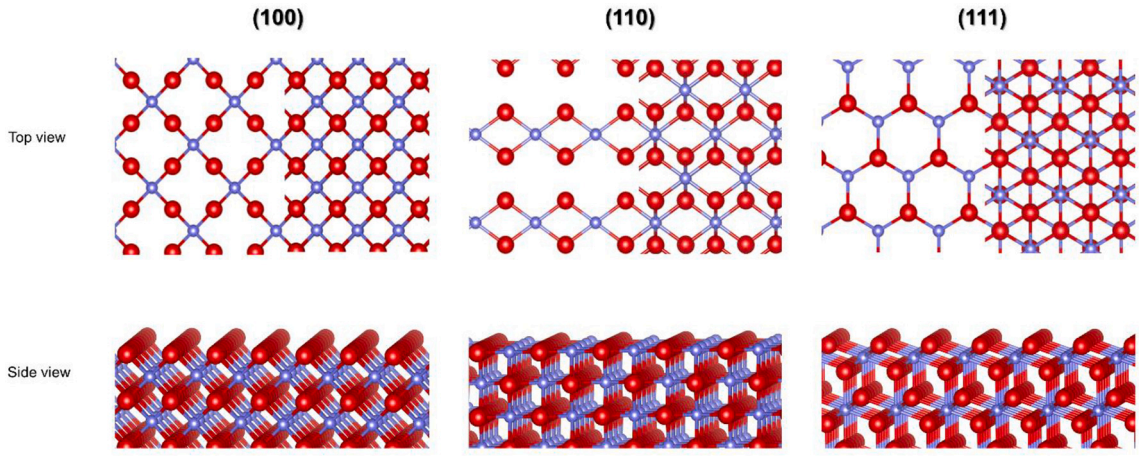

Fig. 6. Representation of the low-index ceria surfaces from top view and side view. Red spheres are O atoms and purple spheres are Ce atoms. In the top view, the left side of each figure represents the top outmost layer only, whereas full projections including subsurface ions are shown in the right side of each figure. The software VESTA [123] was used for creating this image. (For interpretation of the references to colour in this figure legend, the reader is referred to the web version of this article.)

Table 1
Characteristic properties of the low-index ceria surfaces.

Orientation	Tasker classification [108]	Termination	Surface Energy (J/m^2) [124,117,125–127]	Reducibility ranking	Surface site density	
					Ce	O
111	Type-2	Ce and O	0.60–0.71	3rd	$\frac{32}{9\sqrt{3}a^2}$	$\frac{32}{9\sqrt{3}a^2}$
110	Type-1	Ce and O	1.0–1.06	1st	$\frac{\sqrt{2}}{a^2}$	$\frac{2\sqrt{2}}{a^2}$
100	Type-3	Ce or O	1.40–1.44	2nd	$\frac{2}{a^2}$	$\frac{4}{a^2}$

Table 2
Inter-cationic and inter-anionic distances, up to the third neighbor, for the three low index surfaces of ceria. The numbers in parenthesis refer to the number of first, second or third neighbors. The interionic distances and number of neighbors refer to the surface ions only.

Orientation	Ce-Ce distance (and population)			O-O distance (and population)		
	1st neigh.	2nd	3rd	1st neigh.	2nd	3rd
111	$\frac{a}{\sqrt{2}}$ (6)	$\frac{\sqrt{3}a}{\sqrt{2}}$ (6)	$\sqrt{2}a$ (6)	$\frac{a}{\sqrt{2}}$ (6)	$\frac{\sqrt{3}a}{\sqrt{2}}$ (6)	$\sqrt{2}a$ (6)
110	$\frac{a}{\sqrt{2}}$ (2)	a (2)	$\frac{\sqrt{3}a}{\sqrt{2}}$ (4)	$\frac{a}{2}$ (2)	$\frac{a}{\sqrt{2}}$ (2)	$\frac{\sqrt{3}a}{2}$ (4)
100	$\frac{a}{\sqrt{2}}$ (4)	a (4)	$a\sqrt{2}$ (4)	$\frac{a}{2}$ (4)	$\frac{a}{\sqrt{2}}$ (4)	a (4)

mentioned findings, with the binding geometry for carbonate adsorbates being tridentate for (100), bidentate for (110) and monodentate for (111) ceria surfaces. The monodentate configuration for the (111) surface also agrees with the DFT calculations from Kildgaard *et al.* [136], suggesting a monodentate configuration on the (111) nanofacets resulting from the partial reconstruction of the (110) surface under reducing conditions (observed experimentally for ceria nanoparticles at 500 °C [137]). In contrast to these results, recent DFT calculations from Parker and coworkers [124] indicate that the tridentate configuration is the most stable on all ceria surfaces. However, for the conditions of elevated temperatures and low partial pressures typical of SOECs, Vegge and coworkers [138] concluded that tridentate carbonates are unstable over the reduced (111) surface, and a more favorable reaction pathway through a bidentate CO_2^- geometry is suggested.

With respect to the adsorption site, the characteristics of the most favorable site for the carbonate formation are also not well known. A number of DFT studies suggest that the presence of an oxygen vacancy in the proximity of the CO_2 adsorption site energetically favors CO_2 activation. In particular, Vayssilov *et al.* [128] determined that on a model non-stoichiometric ceria nanoparticle the presence of an oxygen vacancy in the immediate vicinity of a carbonate increases the carbonate binding energy, *i.e.* its stability, in the case of both the monodentate and tridentate configuration. Cheng *et al.* [134] suggested that CO_2 chemisorption is favored at an oxygen vacancy site on the reduced CeO_{2-x} (110) surface. On the same surface, Kumari *et al.* [139] also predict that the CO_2 molecule adsorbs in the vicinity of an oxygen vacancy. On the reconstructed CeO_{2-x} (110) surface, Kildgaard *et al.* [136] calculated that the most favorable adsorption site under SOECs operation is on a surface oxygen site having a sub-surface vacancy as the nearest neighbor. These reports suggest a dependence of the CO_2 chemisorption characteristics on the orientation and degree of reduction of the ceria surface. A systematic experimental investigation of the most favorable site for CO_2 chemisorption on different ceria surfaces is nevertheless still lacking.

To sum up, it is well established that the type of reaction intermediate under the reaction conditions typical of SOECs is a carbonate $(CO_3)_{O,\,s}^{'}$. In fact, the presence of the carbonate intermediate in Chueh and co-workers' study [74] is in agreement with what was already observed by Yu *et al.* [140] and, more recently, by Wang [141] and Skafte [62] for both pure and doped ceria-based electrochemical cells under SOEC conditions. However, none of the electrochemical studies mentioned above [62,74,140,141] unequivocally elucidated the configuration of carbonate adsorbed on the ceria (100) surface in the CO_2 electroreduction, and similar experimental studies for the other orientations are still lacking, so that a precise description of the carbonate configuration on the different ceria surface terminations (and its preferential adsorption site) under the operating conditions of SOECs remains an open question. What is clear though is that the carboxylate species $Ce\text{-}CO_2^{\delta-}$ (consisting of a CO_2 adsorbed on top of a Ce cation) typically observed in non-electrochemical low-intermediate temperature catalysis studies [131,142], is detected only in negligible concentrations under SOEC operating conditions up to cathodic overpotentials of ~ −0.3 V [62,74], *i.e.* well beyond the typical polarization in technological SOECs. However, the presence of carboxylate species is observed at very high overpotentials (−0.3 to −0.6 V) in relation to carbon formation [62], as discussed in more detail in Section 2.3.

In the light of the above, it is evident that surface orientations have been extensively studied to understand the type of adsorbate that can form on ceria following CO_2 adsorption, both computationally and experimentally. On the other hand, systematic studies on model systems, clearly correlating the effect of the surface orientation with the electrocatalytic activity of ceria, are lacking. The closest approximation to a model system available in the literature is shape-controlled nanoparticles, such as nanorods, nanocubes and nanooctahedra, which expose different orientations in their facets, as reported in Table 3 and shown for nanocubes in Fig. 8:

Nanoshapes have been vastly employed in the context of heterogeneous catalysis to explore the structure-activity dependence of ceria

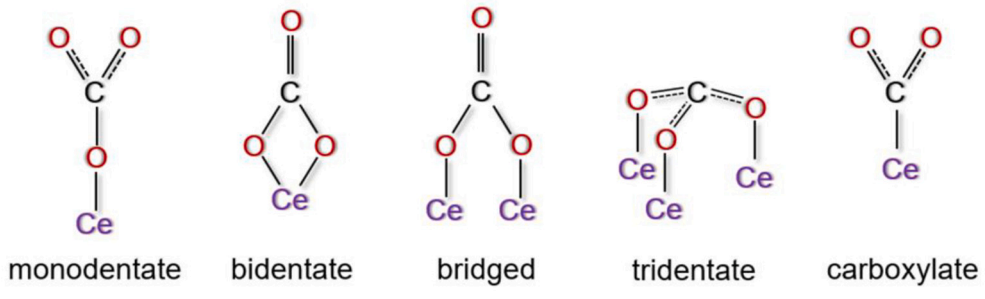

Fig. 7. Schematic representation of the structure of surface carbonates and carboxylates as proposed by earlier studies.

towards different reactions, in both computational [144] and experimental studies [145,146]. The knowledge gained from those studies suggest that indeed the effect of the orientation is significant, and that the different formation energy, concentration and structure of defects resulting from different surface terminations translates into a marked difference in activity of the different nanoshapes. For a number of reactions, including oxidation of CO [147,148] and the synthesis of dimethyl carbonate (DMC) from CO_2 and methanol [149], nanorods were more catalytically active than nanocubes and nanooctahedra [150–155]. This was initially explained with the ranking of orientations with respect to reducibility mentioned earlier: nanocubes expose the (100) facets, nanooctahedra the (111), whereas nanorods were believed to be dominated by the (110) and (100) facets [156]. Thus, the higher activity of nanorods was related to the higher reducibility and lattice oxygen mobility of the (110) surface followed by the (100) and (111) surfaces [157–159]. At a later time, it has been unambiguously demonstrated that nanorods also expose a big portion of (111) surfaces [160], mainly in the form of nanofacets formed upon reconstruction of the reduced (110) surface [161,162]. Crozier *et al.* [163] showed that at temperatures as high as 730 °C in H_2, such reconstructed (111) nanofacets transition back to a smooth bulk-terminated (110) facet: this allow the reduced surface to accommodate the high amount of oxygen vacancies formed upon reduction, without incurring in the formation of a strong perpendicular dipole moment. The presence of this stable and highly-reduced reconstructed (110) surface has been suggested as a possible reason for the observed combination of stability and reactivity observed in nanorods [164]. Other explanations of the superior catalytic activity of rods, instead, point towards a plethora of different special sites that this type of complex nanostructure possesses, such as edges and corners [161] or vacancy clusters [165]. For other catalytic reactions such as hydrogen [166] and ethanol oxidation [167] and reverse water gas shift (RWGS) [168], however, ceria nanocubes showed a higher activity with respect to nanorods. The superior performance of nanocubes is ascribed to the higher inherent reactivity (resulting from their lowest inherent stability) of the (100) surfaces present in cubes compared to the (111) exposed by rods.

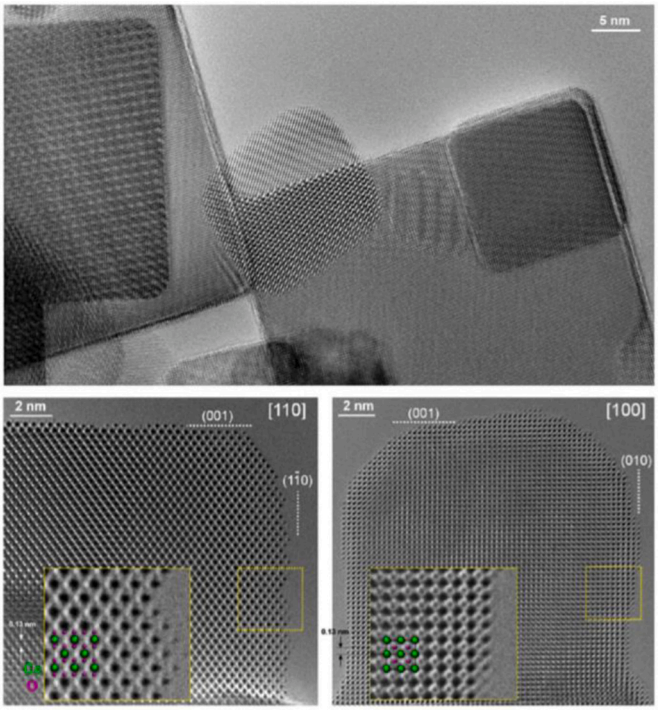

Fig. 8. CeO_2 nanocubes in an environmental transmission electron microscope (ETEM) in ultra-high vacuum. The two images at the bottom are high-resolution transmission electron microscope (HRTEM) bright-field images in [110] and [001] zone axes. Reprinted with permission from *Nano Lett.* 2017, 17, 12, 7652–7658 [143]. Copyright © 2017 American Chemical Society.

Table 3
Low-index surface orientations primarily exposed in different ceria nanoshapes under reducing conditions.

Nanoshape	Orientation primarily exposed
Octahedron	111
Cube	100
Rod	100, 110, 111 (upon reconstruction of 110)

Recently, Symington *et al.* [124] performed DFT calculations on ceria nanoparticles to study the interaction of the low index surface terminations with CO_2 in the context of catalytic applications. Their results, reported in Fig. 9, show that for the entire coverage range investigated, the magnitude of the CO_2 adsorption energy ranks as (100) > (110) > (111), *i.e.* being (100) the most favorable surface for CO_2 adsorption.

Electrocatalytic reactions in SOECs are carried out at higher operating temperatures, which influences the oxygen vacancy and polaron formation, the gas molecules' adsorption/desorption on/from the surface and the stability of the reaction intermediates. DFT calculations by Wu *et al.* [169] for water splitting in SOECs showed that both the turnover frequency (TOF) and the reaction pathway are highly facet-dependent on ceria. The following trend of TOF on the different surface orientations is found for the temperature range between 650 and 900 K: (111) > (110) > (100). For higher temperatures (up to 1200 K), the activity of the (110) and (111) surfaces becomes very similar, but still higher than the (100). The explanation given by the authors is that the formation of the hydroxyl reaction intermediate is more stable on the (100) facet, thus inhibiting the decomposition of the hydroxyl to H_2. With respect to the reaction pathway, for the (100) and (111) facets the reaction always proceeds through an "excessively hydroxylated" surface (*i.e.* when the surface is fully covered in hydroxyls and the reaction thus proceeds through an alternative Ce-H intermediate), whereas for the (110) surface the reaction pathway varies from a fully hydroxylated surface up to 800 K to a partially hydroxylated one at higher temperature.

Experimentally, the shape-dependent electro-catalytic activity of ceria nanoparticles has been investigated for hydrogen oxidation by Tong *et al.* [170]. The authors impregnated ceria nanocubes, nanorods and nanooctahedra into porous $La_{0.9}Sr_{0.1}Ga_{0.8}Mg_{0.2}O_{3-\delta}$ (LSGM) scaffolds and tested them as anode catalysts for intermediate temperature solid oxide fuel cells (IT-SOFCs). Their results showed the activity trend nanorods > nanocubes > nanooctahedra at temperatures below 450 °C.

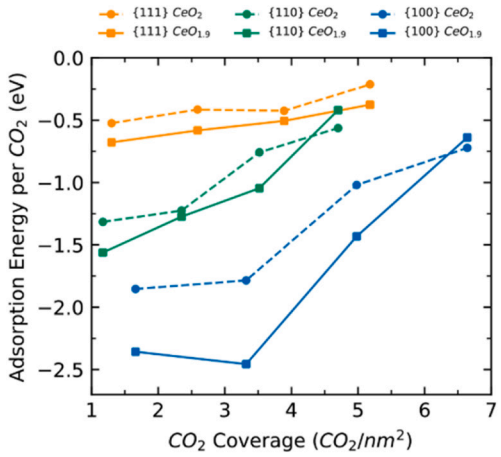

Fig. 9. Adsorption energies for CO_2 adsorbing in the form of a carbonate on the low-index ceria surfaces. Reprinted with permission from *J. Phys. Chem. C* 2020, 124, 42, 23,210–23,220 [124]. Copyright © 2020 American Chemical Society.

However, by increasing temperature to 550 °C, they observed a switch of the highest electrochemical activity towards nanooctahedra, in line with the calculation from Wu *et al.* [169] suggesting the (111) surface (predominantly exposed in nanooctahedra) as the most energetically favored for water splitting at temperature higher than 650 K. However, in addition to direct experimental evidence for the proposed mechanism underlying the observed electrocatalytic behavior, it would be very useful to extend the experimental work to higher temperatures, relevant for HT-SOCs, for both water splitting and CO_2 reduction in SOECs.

An alternative route to study the effect of surface orientation on the electrochemical activity is by employing dense and epitaxial thin films, *e.g.* deposited by PLD onto single crystals with specific orientations. In this approach, the electrode exposes a single, well-defined surface orientation, whose electrocatalytic activity can be probed unequivocally [171]. This approach also offers a means to overcome the challenge of preserving the surface orientation of surface-controlled ceria nanoparticles at high operating temperatures, which can lead to sintering of the nanoparticles and alteration of the exposed facets [137,166,172]. To the best of the authors' knowledge, this type of experimental studies addressing the role of the different ceria low-index surface orientations towards H_2O splitting or CO_2 reduction under SOEC conditions still need to be conducted.

2.2. *Influence of dopants on the electrochemical activity of ceria towards CO_2 reduction*

Cation substitution (doping) of ceria with oxides of metal ions with valences ranging from 2+ to 6+ has been extensively studied. Ceria is a very interesting system for doping, as it is able to maintain its fluorite structure up to ca. 2480 °C (its melting point) over a wide range of pO_2, almost irrespective of the type of cation substitution [69]. The dissolution of oxides of metal ions with lower valences (acceptor dopants) introduces oxygen vacancies in the system, while doping with oxides of metal ions with higher valences (donor dopants) annihilates existing oxygen vacancies. Importantly, doping alters the degree of reducibility of ceria, not only by modifying the oxygen vacancy and Ce^{3+} concentrations, but also the partial molar enthalpy of reduction and the non-configurational entropy, associated with the vibrational frequency of the lattice ions. A comprehensive and detailed overview of the effect of different cation dopants on the defect chemistry, as well as the ionic and electronic conductivity of ceria is provided by Chatzichristodoulou *et al.* in ref. [69].

In ceria, the oxygen transport occurs *via* thermally activated hopping of an oxide ion to a neighboring oxide ion vacancy site. The energy barrier for this mechanism depends on the distance separating the two sites and on the strength of the bond between the oxygen ion and its neighboring cations in the two sites, where this last property is affected in turn by defect-defect and defect-host interactions. Such interactions exist between dopant ions and oxygen vacancies, dopant pairs, oxygen-vacancy pairs, and Ce^{3+}-based defect pairs ($Ce^{3+} - Ce^{3+}$, Ce^{3+} – dopant ions, or Ce^{3+} – oxygen vacancies) [75,96,173], and are the ultimate reason for the limit in ionic conductivity found for high concentrations of substituted cations [84,174,175]. This needs to be taken into consideration when optimizing the doping level of ceria employed as electrocatalyst, since fast ionic transport is needed to retain a constant supply of oxygen vacancies from the bulk to the surface during CO_2 electroreduction (Eq. 3 and 4). Although bulk to surface transport was shown not to be rate limiting for H_2O splitting for an acceptor doped ceria (20 at.% Sm doped ceria) [49,73], the ionic transport could become limiting when ceria is doped with a donor or isovalent dopant.

Doping with a variety of isovalent and aliovalent dopants has been shown by computational studies to reduce the oxygen vacancy formation enthalpy and alter the catalytic properties of the low-index surfaces of ceria. For isovalent dopants, non-redox-active [176] Ti, Zr and Hf have been predicted by Nolan [177] to reduce the oxygen vacancy formation energy on the (110) surface. This is ascribed to the smaller ionic radius of these dopants compared to Ce^{4+}, which results in a distortion of the crystal lattice around the dopant site, weakening the Ce-O bond and making oxygen removal easier. The lower energy of vacancy formation for Zr doping confirms the findings of Mayernick and Janik [178], who calculated a reduced oxygen vacancy formation enthalpy and enhanced methane adsorption for all three low-index ceria surfaces upon Zr doping. The authors also predicted a change in the most favorable surface for oxygen vacancy formation: for a concentration of Zr doping of 3.1%, the trend is (100) > (111) > (110), in contrast with pure ceria where the trend has been shown to be (110) > (100) > (111). More recently, a high number of dopants with an ionic radius similar to that of cerium, at their tetravalent state, have been investigated by Vegge and coworkers [136] for CO_2 reduction under SOEC conditions. Amongst those, Rh, Ir and Pt were found to bond CO noticeably stronger than the undoped ceria surface, a strategy that could potentially enhance the activity of ceria surfaces for CO_2 electroreduction (see Fig. 3). However, Rh, Ir, and Pt doping was predicted to also lower the oxygen vacancy formation energy and thereby also the CO_2 adsorption energy. Since all the relevant free energies were lowered by these dopants, their impact on the relative energy barriers in the reaction landscape was not found to be significant, as can be seen in Fig. 10. It must be noted here that under the high temperature and reducing conditions typical for SOECs, (semi-)noble elements have the tendency to be reduced to their 2+ oxidation state or metallic state [179,180]. This results in reduced solubility limits in the ceria matrix in the former case [181,182], and in the surface decoration of metallic (nano)particles in the latter [183].

KEY POINTS on the role of the surface orientation of ceria in CO_2 reduction in SOECs:

- The stability of the low-index surfaces of ceria is ranked as: (111) > (110) > (100), *i.e.* the (100) being the least stable.
- The reducibility of the three surfaces is ranked instead as: (110) > (100) > (111), *i.e.* a lower energy for the formation of an oxygen vacancy is required on the (110) surface.
- A structure-dependence of the catalytic activity of ceria has been shown for a broad array of reactions in heterogeneous catalysis.
- The surface structure also affects the configuration of the reaction intermediates. For CO_2 reduction in SOECs, the exact configuration of the carbonate CO_3^{2-} (*i.e.* mono-, bi-, poly-dentate or bridged) has not been established experimentally yet.
- The CO_2 adsorption energy is also influenced by the surface orientation: DFT calculations suggest a ranking of (100) > (110) > (111), *i.e.* being (100) the most favorable surface for CO_2 adsorption.
- The influence of surface orientation on the electrochemical performance towards CO_2 reduction under SOEC conditions has not been explored yet, neither experimentally nor theoretically.
- Shape controlled nanoparticles with predominant surface orientations are often used to explore the structure-activity dependence in catalytic reactions. These are not well suited for SOEC studies though, due to possible sintering of the nanoparticles and surface reconstruction/alteration at high temperature and especially in reducing conditions.
- Single crystal thin films offer an alternative approach. The deposition of epitaxial ceria thin films by pulsed laser deposition (PLD) is well established, and offers a means to obtain a well-defined orientation and surface area.

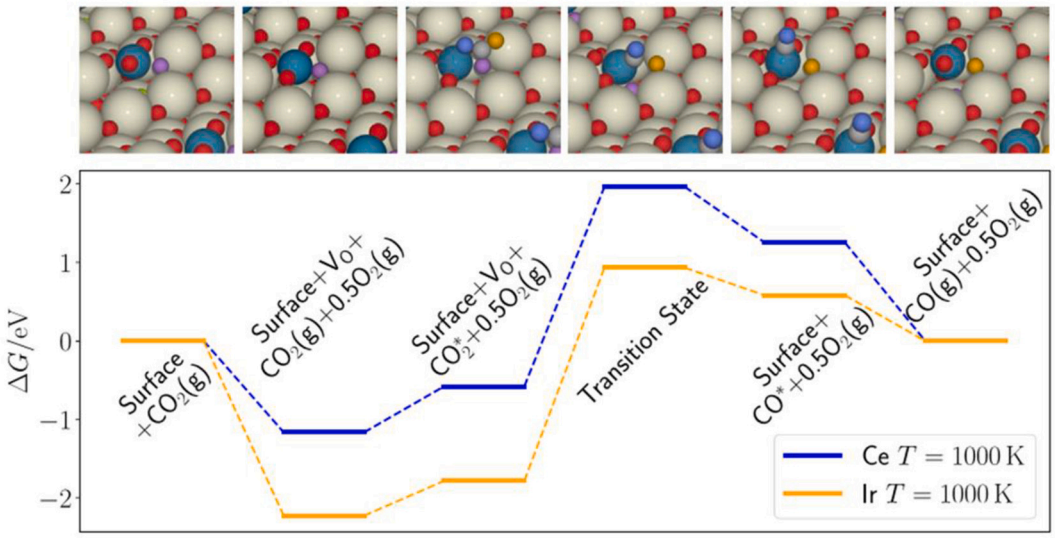

Fig. 10. Energy landscape of CO_2 reduction to CO for the Ir-doped ceria and undoped ceria (110) reconstructed surface. The individual steps are schematically shown in the box above. Gray spheres represent cerium atoms, blue iridium, and red oxygen. Oxygen atoms participating in the surface reactions are represented in arbitrary colors for visual guidance. Reprinted with permission from *Mater. Today Adv.* 2020, 8, 1,001,113 [136]. Copyright © 2020 The Author(s). (For interpretation of the references to colour in this figure legend, the reader is referred to the web version of this article.)

For trivalent dopants, Gd doping was investigated for water splitting in SOECs by Wu *et al.* [184], showing that the energy required to form oxygen vacancies and hydroxyls on the (111) surface is lower for doped ceria with respect to pure ceria. This has also been established experimentally, albeit it should be noted that although the enthalpy for oxygen vacancy formation is reduced, the entropy is also reduced. This results in reduced free energy for oxygen vacancy formation for Gd doped ceria at low to intermediate temperatures but higher at high temperatures [69]. The authors of ref. [184] also showed that incorporation of Gd into the ceria structure makes the surface oxygen vacancy diffusion faster under the conditions of the water splitting reaction. Most importantly though, Gd doping improves the electrocatalytic activity due to the more favorable formation of a Gd-H intermediate compared to the Ce-H one.

The divalent dopants Mg, Ca and Sr have been investigated by DFT calculations by Carey and Nolan [185] on the (111) surface, showing that all dopants promote the formation of additional oxygen vacancies. Amongst these three dopants the oxygen vacancy formation is more facile for Mg, due to its smaller ionic radius introducing a stronger distortion in the lattice. The authors of ref. [185] also found an effect of ionic radius on the activation of methane, where smaller dopants have a beneficial effect, whereas Sr (which has a larger radius over the host cation) worsens the kinetics of the reaction. Other divalent dopants, like Pd and Ni in their partially reduced state, [178,186] were also shown by DFT calculations to lower the energy of formation of additional oxygen vacancies on ceria surfaces, along with reducing the energy barrier for methane adsorption in the case of Pd [178]. A reduced oxygen vacancy formation energy was also calculated for noble metals like Au on all three low-index surfaces [187,188] and Pt on the (111) surface [189]. Recent DFT calculations from Wang *et al.* [190] addressing doping of the (111) surface with V, Cr and Mn also proved lower oxygen vacancy formation energy and lower energy barriers for CO oxidation for all the dopants with respect to undoped ceria. Here again, the low solubility limits of cations with significantly smaller ionic radius than Ce like V, Cr and Mn into the host matrix [182,191] must be taken into consideration.

Besides surface oxygen vacancies, surface Ce^{3+} also play a crucial role in the electrochemical reduction of CO_2 according to the reaction pathway reported in Eq. 3–6. Pentavalent dopants such as Ta and Nb have been proposed as a means to promote Ce^{3+} on the (110) surface [192]. However, the introduction of pentavalent cations in the ceria lattice will also tend to annihilate existing oxygen vacancies, having a detrimental effect to the ion incorporation step associated with or following the carbonate activation. In principle, one could consider co-doping as a potential strategy to couple the effect of different dopants in the electrocatalytic activity of ceria surfaces. In the case of a donor-acceptor-substituted ceria, it was shown experimentally that the two dopants annihilate each other to a large extent, thereby suppressing the formation of charge compensating polarons and oxygen vacancies [193,194]. However, a study combining DFT calculations with thermogravimetric analysis [195] recently introduced a similar dopant strategy for thermochemical H_2O and CO_2 splitting (where a compromise between reducing and oxidizing ability is needed), based on paired charge compensating doped (PCCD) ceria, *e.g.* co-doped with trivalent and pentavalent elements. The effect of the two dopants was demonstrated to be synergistic rather than counteractive for a number of trivalent and pentavalent combinations from the IIIA and VA groups. On the other hand, carefully designed acceptor-acceptor co-doping could offer a marked increase of the oxygen vacancy population, along with local lattice distortions that can promote the reducibility of ceria [69,196]. As an example from the very recent literature, AlKhoori *et al.* [197] found a strong enhancement of the catalytic activity of ceria towards CO oxidation by co-doping with divalent Cu and trivalent Sm.

Experimental studies have been conducted to assess the role of doping in the catalytic activity of ceria towards CO_2 reduction in the context of heterogeneous catalysis. Doping with Mg has been investigated over the (111) ceria surface, where the presence of Mg has been demonstrated to enhance the formation of surface carbonates at room temperature [142]. The reactivity of H_2 pre-reduced 10 at.% Gd and 15 at.% Sm doped-ceria has been tested for chemically driven CO_2 reduction [130], showing that both materials are able to reduce CO_2 to CO, with a similar behavior in terms of both their surface chemistry and redox reactivity. The study of Zhao *et al.* [106], employing CeO_2 and $Ce_{0.5}Zr_{0.5}O_{2-\delta}$ (CZO) nanopowders in a button-cell fixed-bed reactor and H_2 as a reducing agent, showed higher peak rates for CO_2 splitting for CZO at temperatures between 600 and 900 °C, and specifically two-fold higher at 700 °C (61.2 μmole·g^{-1}·s^{-1} for CZO vs. 28.9 μmole·g^{-1}·s^{-1} for ceria). This was ascribed to the much lower oxygen vacancy formation enthalpy for the bulk of CZO (40% lower upon doping with 50 mol% Zr [198]) and the 4-fold higher surface area of CZO, resulting from its enhanced thermal stability. However, at temperatures close to 900 °C, the splitting kinetics are much closer despite the difference in surface

area, and this is ascribed to the higher concentration of surface polarons and oxygen vacancies observed at high temperature for pure ceria compared to CZO (observation later substantiated by another study showing that under H_2 at 800 °C the reducibility of the ceria surface is uninfluenced by increasing the Zr content, in marked contrast with the enhanced reducibility of the bulk [199]). The energy landscape resulting from the kinetic model developed by the authors shows a nearly two-fold higher CO_2 adsorption activation barrier for CeO_2 relative to CZO (starting from the oxidized surface), in line with the different oxygen vacancy formation thermodynamics for the doped and undoped materials. The activation barrier for the charge transfer process (individuated as the rate determining step, Eq. 8) is also somewhat lower for CZO compared to CeO_2 (175 and 216 $kJ{\cdot}mol^{-1}$, respectively). This reflects in the carbonate coverage being more sensitive with the temperature on the ceria surface, in line with the higher concentration of carbonates found on ceria rather than on CZO at temperatures higher than 700 °C.

Turning to electrochemical studies, Gd-doped ceria was preliminary investigated as a promising electrocatalyst for CO_2 electrolysis in SOECs over a decade ago [45], and its excellent activity towards CO_2 reduction, being even higher than towards H_2O splitting in certain instances [200], was more recently confirmed. Amongst Gd-, Y-, La- and Sm-doped ceria in different dopant concentrations, $Sm_{0.2}Ce_{0.8}O_{2-\delta}$ was shown by electrical conductivity relaxation (ECR) to have the highest chemical surface exchange kinetics under reducing conditions (in H_2/Ar mixture) [201]. The effect of the dopant ionic radius on the reducibility of ceria was thoroughly investigated for La, Sm, Gd, and Yb by Yang *et al.* [202], showing an increase of the concentration of surface Ce^{3+} and an enhanced surface reactivity with the decrease of the ionic radius of the dopant cation. Trivalent Eu was also recently proposed as a promising dopant for ceria-based anodes in IT-SOFCs [203].

A number of studies on technological electrodes with different type and amount of dopants in ceria [48,204–209] have also revealed promising activity for CO_2 electroreduction. However, the lack of well-controlled model systems makes it difficult to discern the role of the dopant from other effects, *e.g.* related to the increase of the electrochemically active surface area resulting from nanoparticles loading or to the variability of the electrode microstructure influencing utilization length and gas diffusion contributions. Fundamental studies employing model electrodes with well-defined geometry and surface area, preferably combined with spectroscopy and micro-kinetic modeling, are challenging and thus scarce. However, those type of studies, rather than the ones aiming at maximizing the current density in porous electrodes, are crucial to arrive at a deep atomistic understating of the role of dopants in the electrocatalytic activity of ceria towards CO_2 reduction.

2.3. Influence of strain on the electrochemical activity of ceria towards CO_2 reduction

The role of lattice strain in doped ceria has been extensively investigated in the last decade as a means to overcome the limit in the ionic conductivity imposed by defect-defect interactions for high concentrations of substituted cations [210,211,212], both computationally [213–215] and experimentally by employing thin films and multilayer heterostructures [210,216]. The results of such studies have been summarized in a number of reviews [211,212,217].

Strain can also alter the energy landscape of electrochemical reactions [218,219], according to what is called Mechano-Electro-Chemical (MEC) Coupling [212,220]. In relation to SOCs, extensive experimental work has been carried out on two members of the perovskite family of oxides, namely $La_{1-x}Sr_xMnO_3$ (LSM) and $La_{1-x}Sr_xCoO_3$ (LSC), on the basis of a forerunner DFT study on $LaCoO_3$ (LCO). This last work showed how the energy of vacancy formation on both the bulk and the surface of LCO decreases with increasing tensile strain [221]. Subsequently, both LSM [222] and LSC [223] tensile strained thin films were shown to present a higher oxygen vacancy concentration and faster electron transfer for the oxygen reduction reaction (ORR) on their surfaces, resulting in faster oxygen surface exchange and diffusion in the case of LSC [224]. Later on, reduced energy of oxygen vacancy formation under tensile strain was predicted computationally for both uniaxially [215], biaxially and isotropically [225] strained bulk ceria and isotropically strained bulk CGO [226]. The same trend was also found by DFT calculations for the biaxially strained CeO_2 (100) surface [225] and isotropically strained (111) surface [227]. Very recently, the near-surface of reduced CeO_2 (111) was also investigated by DFT + U calculations to unravel the effect of in-plane strain on the relative stability of surface and subsurface oxygen vacancies [228]. The authors found that while under dilative strain isolated surface vacancies are energetically favored, compressive strain favors isolated subsurface vacancies. For both isolated surface and subsurface oxygen vacancies of CeO_2 (111), Ce^{3+} polarons are next-nearest neighbors (NNN) rather than nearest-neighbors (NN), in line with earlier Scanning-tunneling microscopy (STM) studies and DFT calculations [229], following a lattice relaxation effect to counterbalance the strain introduced by the higher ionic radius of Ce^{3+} compared to Ce^{4+}. The authors of ref. [228] also found that under compressive strain the formation of both surface and subsurface vacancy dimers is favored with respect to the isolated counterparts. The possibility of tuning the presence of vacancy clusters through compressive strain is intriguing, considering that it has been explained as one possible reason for the high catalytic activity of nanorods [165], as reported in section 2.1. Furthermore, the beneficial effect of divacancies has also been predicted for the reduced (110) surface [139], where a lower activation barrier for CO_2 dissociation to CO is found on a divacancy site, with respect to the isolated one. Thus,

KEY POINTS on the role of dopants in ceria for CO_2 reduction in SOECs:

- The oxygen vacancy formation energy on ceria surfaces is lowered by the introduction of smaller sized tetravalent dopants. Tri- and divalent dopants may also lower the enthalpy of formation of oxygen vacancies (beyond those introduced for charge compensation). The reducibility increases as the ionic radius of the dopant decreases.
- In particular for CO_2 electroreduction under SOEC conditions, the introduction of tetravalent Pt, Rh and Ir has been predicted to lower the oxygen vacancy formation energy and to increase the CO adsorption energy at the same time. However, the CO_2 adsorption energy increases as well, limiting the effect on the activation barrier associated with the final charge transfer step.
- Non-redox active tetravalent Zr has been shown to boost the kinetics of chemically driven CO_2 reduction with respect to pure ceria at temperatures lower than 600–700 °C, whereas their behavior is reversed at higher temperatures. The energy barrier for the charge transfer step is lowered for CZO compared to undoped ceria.
- For CO_2 reduction in SOECs, many dopants have shown promising enhancement of the electrochemical activity in technological electrodes. However, many micro-structural parameters can influence the observed performance in porous electrodes with complex morphology. Model electrodes with well-defined surface area and geometry, alleviating the influence of other parameters, are needed to arrive at an atomistic understanding of the role of dopants in the mechanisms governing CO_2 reduction on ceria surfaces.

one could speculate that tensile strain, favoring the reducibility of ceria can enhance the electrocatalytic activity on the (111) surface of pure ceria towards reactions like CO_2 reduction or water splitting. On the other hand, vacancy dimers favored under compressive strain on the (111) surface are possibly responsible for the high catalytic activity of nanorods, and could represent an intriguing method to modulate the electrocatalytic activity of ceria. Turning to the direct effect of strain on activity observed for specific reactions, atomistic simulations on the catalytic activity of ceria nanomaterials towards CO oxidation to CO_2 showed that ceria nanorods oriented along the [110] direction are chemically more reactive under tension than under compression, emphasizing the concrete possibility of tuning the oxide activity *via* lattice strain [230]. More recently, a DFT + *U* study of the electrocatalytic water splitting assessed that the lattice strain is responsible for the shift of the Ce 4f band center, affecting the energy of formation of oxygen vacancies and hydroxyl intermediates [231]. The authors showed how compressive strain (in excess of −3.0%) on the CeO_2 (111) surface reduces the total energy barrier, accelerating the reaction rate towards H_2 evolution at 1200 K. On the same ceria surface, further work from the same group on the CO_2 reduction reaction [138] has shown that the shift of the Ce 4f band center caused by the lattice strain is proportional to the shift in the oxygen vacancy formation energy, which increases under compressive strain and is reduced under dilative strain for all the configurations of Ce^{3+} and oxygen vacancies investigated. Under SOECs conditions, the authors predict that a compressive strain of −4.0% enhances the TOF by 4 orders of magnitude at 800 K, due to the destabilization of the strained CeO_2 (111) surface with respect to the relaxed surface.

Chueh and coworkers [225] recently employed AP-XPS to investigate a set of three $CeO_{2-\delta}$ thin films, one compressively strained on a (100) YSZ substrate (−5.6%), one tensile strained on a (100) $SrTiO_3$ (STO) (2.1%) and one relaxed on a YSZ substrate in H_2/H_2O atmosphere under conditions relevant for SOCs. The authors observed a fourfold increase of the Ce^{3+} concentration on the surface of the strained films compared to the relaxed ones, irrespective of the type of biaxial strain applied. The enthalpy of surface oxygen vacancy formation per O for both compressive and dilative strain was reduced by ~0.4 eV, *i.e.* 15% less that the previously determined 2.9 eV for the surface of a relaxed Sm-doped $CeO_{2-\delta}$ thin film [75]. The authors performed *ab initio* calculations on the ceria bulk to investigate this non-monotonic behavior, and explained it as the combination of two aspects. At 550 °C, on the one hand the authors found that the energy of vacancy formation is lower for tensile strain, due to the larger lattice volume and lowered crystal symmetry, in line with previous computational studies. On the other hand, they found a lower vibrational free energy (*i.e.* higher vibrational entropy) under compressive strain, which along with the better capability of Ce^{3+} to counterbalance the tetragonal distortion introduced by the strain, also favors the formation of oxygen vacancies.

According to this picture, one could assume that the same non-monotonic behavior of strain in enhancing the Ce^{3+} and oxygen vacancy concentrations on ceria surfaces will also apply upon CO_2 reduction under SOECs conditions. Nevertheless, an experimental proof to this assumption and its impact on the reaction rate are still lacking. Here, again, model electrodes produced with PLD offer a way to modulate the strain in the deposited film by choosing substrates of materials with different lattice parameter than ceria. However, it is worthwhile mentioning that ultrathin films of a few nanometers are required to sustain large strain levels [232] and the metal grids typically used as current collector in ceria thin film studies are likely insufficient to guarantee homogeneous polarization in such ultrathin layers [104]. Therefore, for this type of studies efforts must be directed towards new current collector approaches that can help realize homogeneous and well controlled polarization in ceria ultrathin electrodes.

Aside from the case of the ultrathin layers used in fundamental studies, the question arises on the feasibility of sustaining such high levels of strain in real devices. For ceria in particular, critical strain levels of 0.1–0.3% have been predicted for membranes of thicknesses above 10 μm before mechanical failure [90,233,234]. As a reference from recent literature, tensile strain levels approaching 0.5% have been successfully realized in perovskite $La_{0.2}Sr_{0.7}Ni_{0.1}Ti_{0.9}O_{3-\delta}$ (LSNT) thin films with a thickness of 1.3 μm [235]. As an alternative to strain engineering *via* epitaxial growth, vertically aligned nanostructures (VANs) hold promise to stabilize high levels of strain in technological applications [236,237]. Core-shell particles have also been extensively employed to introduce and control strain in bimetallic catalysts [238–240] and, more recently, in oxides [241] and may represent a route to implement strain in SOCs *e.g.* by introduction of strained nanoparticles in the electrode scaffold.

2.4. Surface orientations and dopants as levers to tune the carbon deposition suppression capability of ceria

In the state-of-the-art Ni-YSZ cathodes operating under SOEC conditions, Ni is well known to catalyze the disproportionation of CO into CO_2 and graphite via the Boudouard reaction ($2CO_{(g)} \rightleftharpoons C + CO_{2(g)}$). Graphitic carbon deposits on the electrode active sites reducing the cell performance, and resulting in Ni dusting, which, eventually, can cause the structural failure of the electrode. The effectiveness of ceria in suppressing carbon deposition has been demonstrated by various studies where ceria was introduced as component of the fuel electrode [242]. Amongst others, Duboviks *et al.* [56] showed the beneficial effect of a CGO interlayer on reducing carbon formation in porous Ni/CGO electrodes during CO_2 electrolysis. The same group also proved the carbon deposition suppression capability of Cu-CGO electrodes in electrolysis mode in the context of biogas upgrading [57]. Ceria-coating on Ni structures has been revealed to inhibit carbon deposition in low temperature direct-methane fuel cells [60,243]. Graves and coworkers [61] showed that, for a variety of different compositions of CGO-$Sr_{0.99}Fe_{0.75}Mo_{0.25}O_{3-\delta}$ (SFM) electrodes infiltrated with CGO or Ni-CGO nanoparticles, coking was observable only on Ni-containing cells. By using *operando* vibrational Raman, Welander *et al.* [244] proved that the addition of CGO to a Ni-infiltrated $Sr_{0.94}Ti_{0.9}Nb_{0.1}O_3$ (STN) electrode scaffold decreases the amount of deposited carbon under various CO_2/CH_4 mixtures.

However, recent model electrodes studies have shown that only for strongly cathodic overpotentials at critical CO_2/CO ratios, can carbon deposit on ceria surfaces [62,141,245]. Based on these studies, the mechanism governing the onset of carbon formation on ceria, along with possible strategies to mitigate it, have to a large extent been unraveled. By combination of NAP-XPS and Monte Carlo simulations, Yildiz and coworkers [141] revealed how the introduction of dopants in the ceria structure plays a role in its carbon deposition suppression ability at temperatures relevant for LT-SOEC (450 °C) [141]. Carbon deposition was further suppressed on $Gd_{0.5}Ce_{0.5}O_{1.75}$ and $Zr_{0.5}Ce_{0.5}O_2$ relative to pure or more mildly doped ceria ($Gd_{0.2}Ce_{0.8}O_{1.9}$), with most of the carbon being deposited onto Ce sites rather than on the dopants. The authors individuate the neighboring Ce^{3+}–Ce^{3+} pairs as the catalytic site for carbon deposition from CO (with oxygen sites, filled or vacant, only playing a minor role). Thus, they show that a threshold of [Ce^{3+}] is required at the ceria surface for the onset of carbon formation; since Ce^{3+} and Ce^{4+} arrange alternatingly, Ce^{3+}–Ce^{3+} pairs only become significant above 50% of [Ce^{3+}]/([Ce^{3+}] + [Ce^{4+}] + [dopant]), at which point both pure ceria and $Gd_{0.2}Ce_{0.8}O_{1.9}$ showed the onset of carbon formation. $Gd_{0.5}Ce_{0.5}O_{1.75}$ showed a much lower carbon deposition intensity than the less doped counterpart even when reduced to higher [Ce^{3+}], whereas Zr-doped ceria showed negligible amount of deposited carbon irrespective of the degree of reduction. The carbon suppression capability of the dopants is thus attributed to the fact that the non-redox-active dopant cations impede the formation of Ce^{3+}–Ce^{3+} pairs by "isolating" the Ce^{3+} ions. Importantly, carbon growth saturation was also observed in this work (in agreement with a previous study showing a self-limiting behavior of graphene growth on Cu foils [246]),

KEY POINTS on the role of strain in ceria for CO_2 electroreduction:

- Strain can alter the transport properties of metal oxides like ceria, as well as the energy landscape of electrochemical reactions.
- DFT calculations predict a lower energy of formation of oxygen vacancies for tensile strained ceria, both in the bulk and on the surface.
- Strain is also predicted to modify the relative stability of surface and subsurface vacancies and to influence their aggregation in dimers and clusters.
- For CO_2 reduction in SOECs, compressive strain in excess of −4.0% is predicted to enhance the turnover frequency (TOF) by 4 orders of magnitude at 800 K.
- Experimentally, under a H_2O/H_2 atmosphere relevant for SOECs, both dilative and compressive strain were found to enhance substantially the surface concentration of localized electrons, as well as to lower the surface oxygen vacancy formation energy, compared to the surface of a relaxed sample.
- Experimental studies investigating the effect of strain (and associated enhancement of charge carriers) on the electrochemical activity towards H_2O splitting or CO_2 reduction are still lacking.

with a carbon saturation thickness calculated at 4.2 Å, corresponding to 1–2 monolayers of graphite. The authors also observed a decrease in the peak of the carbonate adsorbate when carbon has deposited. This is in line with what was seen by Skafte *et al.* [62] in their NAP-XPS study, when they pushed the cathodic overpotential beyond the onset of carbon deposition at 500 °C (between −0.3 and − 0.6 V). The depletion of surface carbonates is attributed in both studies to the coverage of the surface by carbon, thus limiting the amount of adsorption sites available for carbonate formation. However, the authors of ref. [62] detected an increase of the peaks corresponding to other oxygenated carbon species (C-O, C=O and/or carboxylate) concomitant to the carbonate peak decrease. Their suggested explanation is that the carbonate coverage facilitates the removal of deposited carbonaceous species, as the carbonates can react to produce carboxylate *via* a reverse Boudouard reaction (Eq. 12).

$$2(CO_3)'_{O,s} + C - C + 2O^x_{O,s} \rightarrow 4CO_2{}^{\delta-} \quad (12)$$

where $O_{O,\ s}{}^{x}$ refers to an adsorbate-free surface oxygen site. If the reaction of Eq. 12 proceeds with sufficiently high rate, it could explain the simultaneous increase of both surface carboxylate species and carbon deposited on the surface of ceria, along with the depletion of carbonate species.

The carbon deposition suppression capability of doped ceria is thus attributed to two different mechanisms according to the two groups of ref. [141] and [62], resulting in different predictions of the effect of surface orientation on carbon deposition. On the one hand, the NAP-XPS-supported DFT calculations by Skafte *et al.* [62] point out that low-index surface orientation play a role in the activity towards carbon deposition. Two main effects connected to surface orientation are suggested to play a role in kinetically preventing C deposition. Firstly, carbon atoms need to be energetically trapped by surface oxygen vacancies as oxidized carbonate intermediates, so that gaseous CO_2 and CO cannot be easily reduced to C. In this sense, a higher oxygen deficiency at the surface is beneficial, and the lower vacancy formation energy for a specific orientation described in Section 2.1 can have a positive effect. Secondly, a high carbonate coverage can facilitate the removal of deposited carbonaceous species according to Eq. 12. Here again, the configuration and concentration of carbonates is connected to the surface orientation. The authors concluded that, based on these requirements, highly oxygen deficient (100) and (110) surface terminations are the best candidates as carbon formation suppressors. On the other end, the authors of ref. [141] claim that the dopant-related carbon deposition inhibition behavior observed for the (100) surface should be in principle similar for the other low-index surface terminations, since the distance between the nearest Ce–Ce pairs (deemed as the catalytic sites for carbon deposition) is the same. However, one could argue that the nearest pair density is different for the three orientations, and this may be playing a role.

In essence, there is now consensus that, even if very high overpotentials are required for the onset of carbon formation, carbon deposition can occur on the surface of ceria [62,141,245]. However, the role of ceria surface orientation with respect to carbon deposition remains unknown as experimental evidence of the electrochemical activity of the different surface orientations towards carbon formation is currently missing.

3. Concluding remarks and future perspective

Electrolysis and co-electrolysis of CO_2 and H_2O in SOECs is envisioned to be the next generation technology for the conversion and storage of electrical energy coming from renewable sources and the production of sustainable fuels and chemicals. One of the main challenges of incorporating SOECs in the energy infrastructure and chemical industry relies in scaling up to the size required by chemical synthesis plants. Alongside, the cell lifetime needs to be improved, especially at high production rates/current densities. Particularly in relation to the fuel electrode, ceria-based materials are considered very promising candidates to address some of the challenges related to the state-of-the-art Ni-YSZ cathode. In order to optimize ceria-based materials for implementation in well-performing and durable electrodes in real devices, the mechanism governing the CO_2 reduction reaction on ceria surfaces needs to be fully understood from a mechanistic point of view. The current status of our understanding of the intrinsic catalytic activity of ceria towards CO_2 reduction has been presented here on the basis of a thorough investigation of related literature, highlighting some important findings that have emerged.

The fundamental role of surface localized electrons and oxygen vacancies for CO_2 reduction has been recognized in a variety of studies, showing that both these species are essential for the charge transfer of the two electrons involved in the reaction [74]. Localized electrons activate the CO_2 molecule during or after adsorption on the ceria surface, with the first electron transfer resulting in the formation of a carbonate as reaction intermediate. Oxygen vacancies play a key role in incorporating one oxygen ion along with the second electron transfer, decomposing the carbonate that subsequently desorbs in the form of gaseous CO. These charge transfer reactions are kinetically limiting the process, each with a relative importance depending on the window of cathodic bias applied. At cathodic overpotentials of −0.1 V, the concentration of adsorbed carbonate intermediates approaches saturation on Sm-doped ceria at 500 °C, a behavior deriving either from strong adsorbate-adsorbate interactions or from the increase of the relative rate of the electron transfer process relative to the formation of the carbonate intermediate. In either case, the final electron transfer process and associated CO desorption appears to be rate limiting for cathodic overpotentials relevant to technological SOEC electrodes.

With respect to carbon deposition, major advancements have been made in understanding the mechanism behind the carbon-tolerance of ceria surfaces. Recent findings have shown that for a ceria-based

KEY POINTS on the role of ceria surface orientations and dopants in suppressing carbon deposition:

- It is well established that ceria offers exceptional carbon suppression capabilities under conditions relevant for SOECs application. However, at sufficiently high overpotentials, carbon does deposit on ceria surface.
- Non-redox active dopants, like Zr and Gd, enhance the carbon suppression capability of ceria, attributed to the fact that their presence isolates the Ce^{3+} ions and impedes the formation of Ce^{3+}–Ce^{3+} pairs, which are deemed as the catalytic sites for carbon deposition.
- Once carbon deposition initiates, the carbonate coverage is suggested to facilitate the removal of deposited carbonaceous species, as the carbonates react with the deposited carbon and surface oxygen ions to produce carboxylate *via* a reverse Boudouard reaction.
- The role of ceria low index surface orientation with respect to carbon deposition prevention remains unexplored; if the mechanism for carbon deposition relies on Ce^{3+}–Ce^{3+} pairs as catalytic sites, the orientation of the surface should not have a substantial effect, since the distance between the nearest Ce–Ce pairs is the same. On the other hand, if the mechanism of carbon deposition is more strongly related to the carbonate formation and coverage, both the different configuration of the adsorbate and oxygen vacancy concentration expected from different orientations would result in a different behavior for the three low index surface terminations, with the 100 and 110 being the best in preventing C-deposition.

electrode the operating conditions in SOECs can be pushed to incredibly high yields of CO products (~95% CO at the outlet, far beyond the limit of the cell stacks used nowadays [247]) before incurring carbon deposition [62]. In the light of this, the persisting uncertainty on the effect of different surface orientations in regards to their capability to influence the inhibition of carbon deposition is perhaps less urgent to address. However, these questions are still very relevant for low temperature SOECs (LT-SOECs), operating in the temperature range between 400 and 650 °C, where the thermodynamic threshold for carbon deposition is shifted to lower CO concentrations. For this operating window, further refinement of our understanding of the mechanism underlying the observed self-limiting behavior of carbon deposition [141] and how this effect can be exploited to tune the carbon–tolerance of ceria, also becomes important.

On the basis of our analysis of the literature available on CO_2 electroreduction in SOEC, accelerating the final electron transfer process and associated CO desorption, is key in improving fuel electrode performance in technological SOEC devices. Promoting the concentration of surface Ce^{3+} while maintaining a sufficiently high concentration of oxygen vacancies is likely to result in improved CO_2 reduction activity. An alternative strategy already proposed [136] is that of weakening the relative adsorption strength of CO_2 to CO on the ceria surface.

Tuning the surface orientation of ceria, the extent and type of doping, and its strain can help tailor the surface of ceria in the direction of accelerating the rate limiting step for CO_2 electroreduction, while maintaining its carbon-deposition suppression capabilities. This requires nevertheless a deeper understanding of the impact of these levers on *e.g.* the surface concentration of defects and adsorbates, and the relative adsorption strength of the latter. Although doping has been investigated in many electrochemical studies employing porous electrodes, the complexity of such systems does not allow for definitive conclusions. In order to understand the role of dopants in the electrochemical reaction, fundamental studies employing model electrodes with well-defined surface area, in which the dopant concentration is systematically modified maintaining unaltered all the other parameters, are crucial. The investigation of strain likewise requires a well-controlled experimental design. Once the effect of strain on the surface electrochemistry of ceria is unraveled, surface engineering through controlled exsolution [248,249], vertically aligned nanostructures (VANs) [236] and core-shell particles [241] may provide methods for controlling and sustaining strain in real SOECs. The effect of the different surface terminations on the electrocatalytic activity of ceria towards CO_2 reduction is another important lever that needs to be further explored, offering also a means of experimentally assessing how well the current understanding of the CO_2 reduction mechanism is portrayed in the measured performance. The variation of surface orientation has the valuable feature that other important parameters, such as doping and strain, are kept constant, while influencing the surface reducibility and oxygen vacancy formation.

Electrochemical kinetic studies making use of model nanostructured electrodes in the form of thin films, combined with *operando* spectroscopic techniques [250], are well-suited for the above discussed purposes. Physical vapor deposition (PVD) techniques such as pulsed laser deposition (PLD) offer a means to vary the parameters in a controlled and systematic manner. Amongst the spectroscopic techniques, near ambient pressure X-ray photoelectron spectroscopy (NAP-XPS) is one of the most valuable, since it combines the advantage of surface sensitivity (with tunable information depth) with information about type and configuration of adsorbates, surface composition, and electronic states, which are all very critical for these studies [251–255]. In the context of fundamental studies employing thin films, efforts must also be directed towards new current collector approaches that can help realize homogeneous and well controlled polarization in the case of ultrathin strained films or less conductive doped ceria, without the disadvantages of the metal grids typically used.

There is no doubt that ceria has great potential as a component in SOEC fuel electrodes, both for H_2O and CO_2 electroreduction. Existing literature has showcased its exceptional electrochemical activity and ability to suppress carbon-deposition. Besides these critical surface functionalities, ceria is also one of the best known MIECs under SOEC fuel electrode conditions, very important in terms of achieving a large utilization thickness in technological electrodes and extending the electrochemically active surface area to the entire two dimensional ceria-gas interface. Furthermore, ceria offers a very flexible platform for tuning its bulk and surface functional properties by means of doping, straining, and nanoshaping. Navigating this immense phase space of possibilities requires a rational approach based on a solid understanding of the mechanistic aspects of the electrochemical reaction of interest and of the role of these tunable parameters. We hope that this review, extracting established understanding gained after decades of research efforts, will provide a useful springboard for further progress in this direction.

Declaration of Competing Interest

The authors declare that they have no known competing financial interests or personal relationships that could have appeared to influence the work reported in this paper.

Acknowledgments

This work was supported by a research grant (9455) from VILLUM FONDEN. E.M.S. gratefully acknowledges Prof. Heine Anton Hansen for helpful insights on the carbonate adsorption geometry and Dr. Francesco Chiabrera for fruitful discussions and feedback on the manuscript.

References

[1] IEA, CO2 Emissions from Fuel Combustion: Overview, IEA, Paris, 2020. https://www.iea.org/reports/co2-emissions-from-fuel-combustion-overview. Accessed: 28/6/2021.

[2] IEA, The Future of Petrochemicals. https://www.iea.org/reports/the-future-of-petrochemicals, 2018. Accessed: 28/6/2021.

[3] S.D. Ebbesen, S.H. Jensen, A. Hauch, M.B. Mogensen, High temperature electrolysis in alkaline cells, solid proton conducting cells, and solid oxide cells, Chem. Rev. 114 (2014) 10697–10734.

[4] A. Hauch, S.D. Ebbesen, S.H. Jensen, M. Mogensen, Highly efficient high temperature electrolysis, J. Mater. Chem. 18 (2008) 2331.

[5] Q. Fu, C. Mabilat, M. Zahid, A. Brisse, L. Gautier, Syngas production via high-temperature steam/CO2 co-electrolysis: an economic assessment, Energy Environ. Sci. 3 (2010) 1382.

[6] A. Hauch, et al., Recent advances in solid oxide cell technology for electrolysis, Science 370 (2020) 10.

[7] H. Shimada, et al., Nanocomposite electrodes for high current density over 3 A cm−2 in solid oxide electrolysis cells, Nat. Commun. 10 (2019).

[8] Y. Zheng, Solid Oxide Electrolysis of H2O and CO2 to Produce Hydrogen and Low-Carbon Fuels, Electrochem. Energy Rev. 10 (2021).

[9] X. Zhang, Y. Song, G. Wang, X. Bao, Co-electrolysis of CO2 and H2O in high-temperature solid oxide electrolysis cells: Recent advance in cathodes, J. Energy Chem. 26 (2017) 839–853.

[10] M.B. Mogensen, et al., Reversible solid-oxide cells for clean and sustainable energy, Clean Energy 3 (2019) 175–201.

[11] S. Biswas, A.P. Kulkarni, S. Giddey, S. Bhattacharya, A review on synthesis of methane as a pathway for renewable energy storage with a focus on solid oxide electrolytic cell-based processes, Front. Energy Res. 8 (2020), 570112.

[12] S. Gunduz, D.J. Deka, U.S. Ozkan, Advances in high-temperature electrocatalytic reduction of CO_2 and H_2O, Adv. Catal. 62 (2018) 113–165. Elsevier.

[13] Y. Jiang, F. Chen, C. Xia, A review on cathode processes and materials for electro-reduction of carbon dioxide in solid oxide electrolysis cells, J. Power Sources 22 (2021).

[14] R. Küngas, et al., Progress in SOEC Development Activities at Haldor Topsøe, ECS Trans. 91 (2019) 215–223.

[15] L. Wang, et al., Power-to-fuels via solid-oxide electrolyzer: Operating window and techno-economics, Renew. Sust. Energ. Rev. 110 (2019) 174–187.

[16] M. Reytier, et al., Stack performances in high temperature steam electrolysis and co-electrolysis, Int. J. Hydrog. Energy 40 (2015) 11370–11377.

[17] J.B. Hansen, Solid oxide electrolysis – a key enabling technology for sustainable energy scenarios, Faraday Discuss. 182 (2015) 9–48.

[18] M. Marchese, E. Giglio, M. Santarelli, A. Lanzini, Energy performance of Power-to-Liquid applications integrating biogas upgrading, reverse water gas shift, solid oxide electrolysis and Fischer-Tropsch technologies, Energy Convers. Manag. X 6 (2020), 100041.

[19] G. Lorenzi, A. Lanzini, M. Santarelli, A. Martin, Exergo-economic analysis of a direct biogas upgrading process to synthetic natural gas via integrated high-temperature electrolysis and methanation, Energy 141 (2017) 1524–1537.

[20] L.R. Clausen, G. Butera, S.H. Jensen, High Efficiency SNG Production from Biomass and Electricity by Integrating Gasification with Pressurized Solid Oxide Electrolysis Cells. 15, 2019.

[21] J.B. Hansen, F. Fock, H.H. Lindboe, Biogas upgrading: by steam electrolysis or co-electrolysis of biogas and steam, ECS Trans. 57 (2013) 3089–3097.

[22] S. Rasi, A. Veijanen, J. Rintala, Trace compounds of biogas from different biogas production plants, Energy 32 (2007) 1375–1380.

[23] S. Ali, K. Sørensen, M.P. Nielsen, Modeling a novel combined solid oxide electrolysis cell (SOEC) - Biomass gasification renewable methanol production system, Renew. Energy 154 (2020) 1025–1034.

[24] F. Salomone, et al., Techno-economic modelling of a Power-to-Gas system based on SOEC electrolysis and CO2 methanation in a RES-based electric grid, Chem. Eng. J. 377 (2019), 120233.

[25] Z. Chehade, C. Mansilla, P. Lucchese, S. Hilliard, J. Proost, Review and analysis of demonstration projects on power-to-X pathways in the world, Int. J. Hydrog. Energy 44 (2019) 27637–27655.

[26] A.O. Isenberg, Three-man Solid Electrolyte Carbon Dioxide Electrolysis Breadboard, 1989.

[27] https://mars.nasa.gov/mars2020/spacecraft/instruments/moxie/. Accessed: 28/6/21.

[28] J.K. Nørskov, A. Latimer, C.F. Dickens, K. Nielsen, Research Needs Towards Sustainable Production of Fuels and Chemicals. https://www.energy-x.eu/research-needs-report/, 2019.

[29] T. Burdyny, W.A. Smith, CO_2 reduction on gas-diffusion electrodes and why catalytic performance must be assessed at commercially-relevant conditions, Energy Environ. Sci. 12 (2019) 1442–1453.

[30] R.J. Lim, et al., A review on the electrochemical reduction of CO2 in fuel cells, metal electrodes and molecular catalysts, Catal. Today 233 (2014) 169–180.

[31] S. Nitopi, et al., Progress and perspectives of electrochemical CO_2 reduction on copper in aqueous electrolyte, Chem. Rev. 119 (2019) 7610–7672.

[32] A. Alcasabas, P.R. Ellis, I. Malone, G. Williams, C. Zalitis, The Conversion of Carbon Dioxide into Useful Products: Part I, 2021, p. 17.

[33] R. Küngas, Review—Electrochemical CO $_2$ Reduction for CO Production: Comparison of Low- and High-Temperature Electrolysis Technologies, J. Electrochem. Soc. 167 (2020), 044508.

[34] V. Kaplan, E. Wachtel, K. Gartsman, Y. Feldman, I. Lubomirsky, Conversion of CO2 to CO by electrolysis of molten lithium carbonate, J. Electrochem. Soc. 157 (2010) B552–B556.

[35] V. Kaplan, E. Wachtel, I. Lubomirsky, CO_2 to CO electrochemical conversion in molten Li_2CO_3 is stable with respect to sulfur contamination, J. Electrochem. Soc. 161 (2014) F54–F57.

[36] Y. Song, X. Zhang, K. Xie, G. Wang, X. Bao, High-temperature CO $_2$ electrolysis in solid oxide electrolysis cells: developments, challenges, and prospects, Adv. Mater. 31 (2019), 1902033.

[37] M.B. Mogensen, et al., Comprehensive hypotheses for degradation mechanisms in Ni-stabilized zirconia electrodes, ECS Trans. 91 (2019) 613–620.

[38] L. Ye, K. Xie, High-temperature electrocatalysis and key materials in solid oxide electrolysis cells, J. Energy Chem. 54 (2021) 736–745.

[39] S.D. Ebbesen, M. Mogensen, Electrolysis of carbon dioxide in solid oxide electrolysis cells, J. Power Sources 193 (2009) 349–358.

[40] Z. Zhan, et al., Syngas production by coelectrolysis of CO_2/H_2O: the basis for a renewable energy cycle, Energy Fuel 23 (2009) 3089–3096.

[41] Y. Tao, S.D. Ebbesen, M.B. Mogensen, Carbon deposition in solid oxide cells during co-electrolysis of H_2O and CO_2, J. Electrochem. Soc. 161 (2014) F337–F343.

[42] M.S. Khan, et al., Fundamental mechanisms involved in the degradation of nickel–yttria stabilized zirconia (Ni–YSZ) anode during solid oxide fuel cells operation: a review, Ceram. Int. 42 (2016) 35–48.

[43] M. Trini, et al., Comparison of microstructural evolution of fuel electrodes in solid oxide fuel cells and electrolysis cells, J. Power Sources 450 (2020), 227599.

[44] M.B. Mogensen, et al., Ni migration in solid oxide cell electrodes: review and revised hypothesis, Fuel Cells 21 (2021) 415–429.

[45] R. Green, C. Liu, S. Adler, Carbon dioxide reduction on gadolinia-doped ceria cathodes, Solid State Ionics 179 (2008) 647–660.

[46] X. Yue, J.T.S. Irvine, Alternative cathode material for CO_2 reduction by high temperature solid oxide electrolysis cells, J. Electrochem. Soc. 159 (2012) F442–F448.

[47] X. Yue, J.T.S. Irvine, Modification of LSCM–GDC cathodes to enhance performance for high temperature CO_2 electrolysis using solid oxide electrolysis cells (SOECs), J. Mater. Chem. A 5 (2017) 7081–7090.

[48] C.-Y. Cheng, G.H. Kelsall, L. Kleiminger, Reduction of CO2 to CO at Cu–ceria-gadolinia (CGO) cathode in solid oxide electrolyser, J. Appl. Electrochem. 43 (2013) 1131–1144.

[49] W.C. Chueh, Y. Hao, W. Jung, S.M. Haile, High electrochemical activity of the oxide phase in model ceria–Pt and ceria–Ni composite anodes, Nat. Mater. 11 (2012) 155–161.

[50] Stephen J. Skinner, John A. Kilner, Oxygen ion conductors, Mater. Today 6 (2003) 30–37.

[51] P. Kim-Lohsoontorn, J. Bae, Electrochemical performance of solid oxide electrolysis cell electrodes under high-temperature coelectrolysis of steam and carbon dioxide, J. Power Sources 196 (2011) 7161–7168.

[52] V. Singh, et al., Feasibility of alternative electrode materials for high temperature CO2 reduction on solid oxide electrolysis cell, J. Power Sources 293 (2015) 642–648.

[53] S. Ovtar, et al., Boosting the Performance and Durability of Ni/YSZ Cathode for Hydrogen Production at High Current Densities via Decoration with Nano-sized Electrocatalysts. 13, 2019.

[54] A. Nenning, M. Holzmann, J. Fleig, A.K. Opitz, Excellent kinetics of single-phase Gd-doped ceria fuel electrodes in solid oxide cells, Mater. Adv. 2 (2021) 5422–5431.

[55] E. Ramírez-Cabrera, The influence of point defects on the resistance of ceria to carbon deposition in hydrocarbon catalysis, Solid State Ionics 136–137 (2000) 825–831.

[56] V. Duboviks, et al., A Raman spectroscopic study of the carbon deposition mechanism on Ni/CGO electrodes during CO/CO $_2$ electrolysis, Phys. Chem. Chem. Phys. 16 (2014) 13063–13068.

[57] V. Duboviks, et al., Carbon deposition behaviour in metal-infiltrated gadolinia doped ceria electrodes for simulated biogas upgrading in solid oxide electrolysis cells, J. Power Sources 293 (2015) 912–921.

[58] S. Park, J.M. Vohs, R.J. Gorte, Direct oxidation of hydrocarbons in a solid-oxide fuel cell, Nature 404 (2000) 265–267.

[59] W.C. Chueh, S.M. Haile, Ceria as a thermochemical reaction medium for selectively generating syngas or methane from H_2O and CO_2, ChemSusChem 2 (2009) 735–739.

[60] J.G. Lee, et al., Durable and high-performance direct-methane fuel cells with coke-tolerant ceria-coated Ni catalysts at reduced temperatures, Electrochim. Acta 191 (2016) 677–686.

[61] T.L. Skafte, B.R. Sudireddy, P. Blennow, C. Graves, Carbon and redox tolerant infiltrated oxide fuel-electrodes for solid oxide cells, ECS Trans. 72 (2016) 201–214.

[62] T.L. Skafte, et al., Selective high-temperature CO2 electrolysis enabled by oxidized carbon intermediates, Nat. Energy 4 (2019) 846–855.

[63] H. Kurokawa, T.Z. Sholklapper, C.P. Jacobson, L.C. De Jonghe, S.J. Visco, Ceria nanocoating for sulfur tolerant ni-based anodes of solid oxide fuel cells, Electrochem. Solid-State Lett. 10 (2007) B135.

[64] J.W. Yun, S.P. Yoon, S. Park, H.S. Kim, S.W. Nam, Analysis of the regenerative H2S poisoning mechanism in Ce0.8Sm0.2O2-coated Ni/YSZ anodes for intermediate temperature solid oxide fuel cells, Int. J. Hydrog. Energy 36 (2011) 787–796.

[65] H. He, R.J. Gorte, J.M. Vohs, Highly sulfur tolerant Cu-ceria anodes for SOFCs, Electrochem. Solid-State Lett. 8 (2005) A279.

[66] W. Jung, J.O. Dereux, W.C. Chueh, Y. Hao, S.M. Haile, High electrode activity of nanostructured, columnar ceria films for solid oxide fuel cells, Energy Environ. Sci. 5 (2012) 8682.
[67] C. Sun, H. Li, L. Chen, Nanostructured ceria-based materials: synthesis, properties, and applications, Energy Environ. Sci. 5 (2012) 8475.
[68] L. Zhang, et al., Nano-CeO_2 -modified cathodes for direct electrochemical CO_2 reduction in solid oxide electrolysis cells, ACS Sustain. Chem. Eng. 7 (2019) 9629–9636.
[69] C. Chatzichristodoulou, P.T. Blennow, M. Søgaard, P.V. Hendriksen, M. B. Mogensen, Ceria and its use in solid oxide cells and oxygen membranes, Catal. Sci. Ser. 12 (2013) 623–782. IMPERIAL COLLEGE PRESS.
[70] S. Sanna, et al., Fabrication and electrochemical properties of epitaxial samarium-doped ceria films on $SrTiO_3$ -buffered MgO substrates, Adv. Funct. Mater. 19 (2009) 1713–1719.
[71] N. Yang, et al., Role of associated defects in oxygen ion conduction and surface exchange reaction for epitaxial samaria-doped ceria thin films as catalytic coatings, ACS Appl. Mater. Interfaces 8 (2016) 14613–14621.
[72] W.C. Chueh, S.M. Haile, Electrochemical studies of capacitance in cerium oxide thin films and its relationship to anionic and electronic defect densities, Phys. Chem. Chem. Phys. 11 (2009) 8144.
[73] Z.A. Feng, F. El Gabaly, X. Ye, Z.-X. Shen, W.C. Chueh, Fast vacancy-mediated oxygen ion incorporation across the ceria–gas electrochemical interface, Nat. Commun. 5 (2014) 4374.
[74] Z.A. Feng, M.L. Machala, W.C. Chueh, Surface electrochemistry of CO_2 reduction and CO oxidation on Sm-doped CeO_{2-x}: coupling between Ce^{3+} and carbonate adsorbates, Phys. Chem. Chem. Phys. 17 (2015) 12273–12281.
[75] W.C. Chueh, et al., Highly enhanced concentration and stability of reactive Ce^{3+} on doped CeO_2 surface revealed in operando, Chem. Mater. 24 (2012) 1876–1882.
[76] Y. Choi, et al., Unravelling inherent electrocatalysis of mixed-conducting oxide activated by metal nanoparticle for fuel cell electrodes, Nat. Nanotechnol. 14 (2019) 245–251.
[77] P. Velicsanyi, et al., The effect of Mn Co-doping on the electrochemical properties of Gd0.2Ce0.8O1.9-d/Pt model-composite electrodes, ECS Trans. 68 (2015) 1509–1516.
[78] A. Nenning, A. Opitz, Low oxygen partial pressure increases grain boundary ion conductivity in Gd-doped ceria thin films, J. Phys. Energy 2 (2019), 014002.
[79] J. Fleig, et al., Thin film microelectrodes in SOFC electrode research, Fuel Cells 6 (2006) 284–292.
[80] K. Reed, et al., Exploring the properties and applications of nanoceria: is there still plenty of room at the bottom? Environ. Sci. Nano. 1 (2014) 390–405.
[81] T. Montini, M. Melchionna, M. Monai, P. Fornasiero, Fundamentals and catalytic applications of CeO_2 -Based Materials, Chem. Rev. 116 (2016) 5987–6041.
[82] C. Xu, X. Qu, Cerium oxide nanoparticle: a remarkably versatile rare earth nanomaterial for biological applications, NPG Asia Mater. 6 (2014) e90.
[83] L. Vivier, D. Duprez, Ceria-based solid catalysts for organic chemistry, ChemSusChem 3 (2010) 654–678.
[84] M. Mogensen, Physical, chemical and electrochemical properties of pure and doped ceria, Solid State Ionics 129 (2000) 63–94.
[85] H.L. Tuller, S.R. Bishop, Point defects in oxides: tailoring materials through defect engineering, Annu. Rev. Mater. Res. 41 (2011) 369–398.
[86] J. Paier, C. Penschke, J. Sauer, Oxygen defects and surface chemistry of ceria: quantum chemical studies compared to experiment, Chem. Rev. 113 (2013) 3949–3985.
[87] D.R. Mullins, The surface chemistry of cerium oxide, Surf. Sci. Rep. 70 (2015) 42–85.
[88] M. Coduri, S. Checchia, M. Longhi, D. Ceresoli, M. Scavini, Rare earth doped ceria: the complex connection between structure and properties, Front. Chem. 6 (2018) 526.
[89] R. Schmitt, et al., A review of defect structure and chemistry in ceria and its solid solutions, Chem. Soc. Rev. 49 (2020) 554–592.
[90] S.R. Bishop, et al., Chemical expansion: implications for electrochemical energy storage and conversion devices, Annu. Rev. Mater. Res. 44 (2014) 205–239.
[91] C. Chatzichristodoulou, P. Norby, P.V. Hendriksen, M.B. Mogensen, Size of oxide vacancies in fluorite and perovskite structured oxides, J. Electroceram. 34 (2015) 100–107.
[92] A.F. Zurhelle, X. Tong, A. Klein, D.S. Mebane, R.A.D. Souza, A space-charge treatment of the increased concentration of reactive species at the surface of a ceria solid solution, Angew. Chem. Int. Ed. 5 (2017).
[93] M. Boaro, S. Colussi, A. Trovarelli, Ceria-based materials in hydrogenation and reforming reactions for CO2 valorization, Front. Chem. 7 (2019) 28.
[94] K. Chang, H. Zhang, M. Cheng, Q. Lu, Application of ceria in CO_2 conversion catalysis, ACS Catal. 10 (2020) 613–631.
[95] F.A. Kröger, H.J. Vink, Relations between the concentrations of imperfections in crystalline solids, Solid State Phys. 3 (1956) 307–435. Elsevier.
[96] Friedrich Esch, et al., Electron localization determines defect formation on ceria substrates, Science 309 (2005) 752–755.
[97] S. Gritschneder, M. Reichling, Structural elements of CeO_2 (111) surfaces, Nanotechnology 18 (2007), 044024.
[98] D. Marrocchelli, B. Yildiz, First-principles assessment of H_2S and H_2O reaction mechanisms and the subsequent hydrogen absorption on the CeO_2 (111) surface, J. Phys. Chem. C 116 (2012) 2411–2424.
[99] M.B. Watkins, A.S. Foster, A.L. Shluger, Hydrogen cycle on CeO_2 (111) surfaces: density functional theory calculations, J. Phys. Chem. C 111 (2007) 15337–15341.
[100] H.A. Hansen, C. Wolverton, Kinetics and thermodynamics of H_2O dissociation on reduced CeO_2 (111), J. Phys. Chem. C 118 (2014) 27402–27414.
[101] C. Zhang, et al., Mechanistic Studies of water electrolysis and hydrogen electro-oxidation on high temperature ceria-based solid oxide electrochemical cells, J. Am. Chem. Soc. 135 (2013) 11572–11579.
[102] Z.A. Feng, et al., Origin of overpotential-dependent surface dipole at CeO_{2-x}/gas interface during electrochemical oxygen insertion reactions, Chem. Mater. 28 (2016) 6233–6242.
[103] C. Chen, D. Chen, W.C. Chueh, F. Ciucci, Modeling the impedance response of mixed-conducting thin film electrodes, Phys. Chem. Chem. Phys. 16 (2014) 11573.
[104] J. Liu, F. Ciucci, Modeling the impedance spectra of mixed conducting thin films with exposed and embedded current collectors, Phys. Chem. Chem. Phys. 19 (2017) 26310–26321.
[105] K.R. Hahn, M. Iannuzzi, A.P. Seitsonen, J. Hutter, Coverage effect of the CO_2 adsorption mechanisms on CeO_2 (111) by first principles analysis, J. Phys. Chem. C 117 (2013) 1701–1711.
[106] Z. Zhao, M. Uddi, N. Tsvetkov, B. Yildiz, A.F. Ghoniem, Enhanced intermediate-temperature CO_2 splitting using nonstoichiometric ceria and ceria–zirconia, Phys. Chem. Chem. Phys. 19 (2017) 25774–25785.
[107] A.K. Opitz, et al., Surface chemistry of perovskite-type electrodes during high temperature CO_2 electrolysis investigated by *Operando* photoelectron spectroscopy, ACS Appl. Mater. Interfaces 9 (2017) 35847–35860.
[108] P.W. Tasker, The stability of ionic crystal surfaces, J. Phys. C Solid State Phys. 12 (1979) 4977–4984.
[109] G.S. Herman, Surface structure determination of CeO_2 (001) by angle-resolved mass spectroscopy of recoiled ions, Phys. Rev. B 59 (1999) 14899–14902.
[110] Y. Pan, et al., Ceria nanocrystals exposing wide (100) facets: structure and polarity compensation, Adv. Mater. Interfaces 1 (2014), 1400404.
[111] C. Yang, et al., Surface refaceting mechanism on cubic ceria, J. Phys. Chem. Lett. 11 (2020) 7925–7931.
[112] Y. Shi, et al., Surface structure of coherently strained ceria ultrathin films, Phys. Rev. B 94 (2016), 205420.
[113] Z. Yang, T.K. Woo, M. Baudin, K. Hermansson, Atomic and electronic structure of unreduced and reduced CeO2 surfaces: a first-principles study, J. Chem. Phys. 120 (2004) 7741–7749.
[114] Y. Jiang, J.B. Adams, M. van Schilfgaarde, Density-functional calculation of CeO2 surfaces and prediction of effects of oxygen partial pressure and temperature on stabilities, J. Chem. Phys. 123 (2005), 064701.
[115] T. Désaunay, A. Ringuedé, M. Cassir, F. Labat, C. Adamo, Modeling basic components of solid oxide fuel cells using density functional theory: bulk and surface properties of CeO_2, Surf. Sci. 606 (2012) 305–311.
[116] M. Nolan, S. Grigoleit, D.C. Sayle, S.C. Parker, G.W. Watson, Density functional theory studies of the structure and electronic structure of pure and defective low index surfaces of ceria, Surf. Sci. 576 (2005) 217–229.
[117] M. Nolan, S.C. Parker, G.W. Watson, The electronic structure of oxygen vacancy defects at the low index surfaces of ceria, Surf. Sci. 595 (2005) 223–232.
[118] T.X.T. Sayle, Stephen C. Parker, Richard A. Catlow, Surface oxygen vacancy formation on CeO_2 and its role in the oxidation of carbon monoxide, J. Chem. Soc. Chem. Commun. (1992) 977–978.
[119] J.C. Conesa, Computer modeling of surfaces and defects on cerium dioxide, Surf. Sci. 339 (1995) 337–352.
[120] H.-T. Chen, Y.M. Choi, M. Liu, M.C. Lin, A theoretical study of surface reduction mechanisms of CeO_2(111) and (110) by H_2, ChemPhysChem 8 (2007) 849–855.
[121] N.V. Skorodumova, M. Baudin, K. Hermansson, Surface properties of CeO_2 from first principles, Phys. Rev. B 69 (2004), 075401.
[122] W. Yuan, S.M. Haile, Insensitivity of the extent of surface reduction of ceria on termination: comparison of (001), (110), and (111) faces, MRS Commun. 10 (2020) 636–641.
[123] K. Momma, F. Izumi, VESTA 3 for Three-dimensional Visualization of Crystal, Volumetric and Morphology Data. 5, 2011.
[124] A.R. Symington, R.M. Harker, M.T. Storr, M. Molinari, S.C. Parker, Thermodynamic evolution of cerium oxide nanoparticle morphology using carbon dioxide, J. Phys. Chem. C 124 (2020) 23210–23220.
[125] S. Gennard, F. Corà, C.R.A. Catlow, Comparison of the bulk and surface properties of ceria and zirconia by ab initio investigations, J. Phys. Chem. B 103 (1999) 10158–10170.
[126] M. Molinari, S.C. Parker, D.C. Sayle, M.S. Islam, Water adsorption and its effect on the stability of low index stoichiometric and reduced surfaces of ceria, J. Phys. Chem. C 116 (2012) 7073–7082.
[127] A.R. Symington, et al., strongly bound surface water affects the shape evolution of cerium oxide nanoparticles, J. Phys. Chem. C 124 (2020) 3577–3588.
[128] G.N. Vayssilov, M. Mihaylov, P.St. Petkov, K.I. Hadjiivanov, K.M. Neyman, Reassignment of the vibrational spectra of carbonates, formates, and related surface species on ceria: a combined density functional and infrared spectroscopy investigation, J. Phys. Chem. C 115 (2011) 23435–23454.
[129] F. Bozon-Verduraz, A. Bensalem, IR studies of cerium dioxide: influence of impurities and defects, J. Chem. Soc. Faraday Trans. 90 (1994) 653.
[130] M. Grünbacher, B. Klötzer, S. Penner, CO_2 reduction by hydrogen pre-reduced acceptor-doped ceria, ChemPhysChem 20 (2019) 1706–1718.
[131] C. Li, et al., Carbon monoxide and carbon dioxide adsorption on cerium oxide studied by Fourier-transform infrared spectroscopy. Part 1.—Formation of carbonate species on dehydroxylated CeO2, at room temperature, J. Chem. Soc. Faraday Trans. 1 Phys. Chem. Condens. Phases 85 (1989) 929.
[132] S. Chen, et al., Probing surface structures of CeO_2, TiO_2, and Cu_2O nanocrystals with CO and CO_2 chemisorption, J. Phys. Chem. C 120 (2016) 21472–21485.

[133] P.M. Albrecht, D. Jiang, D.R. Mullins, CO_2 adsorption as a flat-lying, tridentate carbonate on CeO_2 (100), J. Phys. Chem. C 118 (2014) 9042–9050.
[134] Z. Cheng, B.J. Sherman, C.S. Lo, Carbon dioxide activation and dissociation on ceria (110): a density functional theory study, J. Chem. Phys. 138 (2013), 014702.
[135] K.R. Hahn, A.P. Seitsonen, M. Iannuzzi, J. Hutter, Functionalization of CeO_2 (111) by deposition of small Ni clusters: effects on CO_2 adsorption and O vacancy formation, ChemCatChem 7 (2015) 625–634.
[136] J.V. Kildgaard, H.A. Hansen, T. Vegge, DFT+U study of CO_2 reduction and CO oxidation on a reconstructed CeO_2−(110) facet, Mater. Today Adv. 8 (2020), 100111.
[137] O.S. Bezkrovnyi, P. Kraszkiewicz, M. Ptak, L. Kepinski, Thermally induced reconstruction of ceria nanocubes into zigzag {111}-nanofacetted structures and its influence on catalytic activity in CO oxidation, Catal. Commun. 117 (2018) 94–98.
[138] J.V. Kildgaard, H.A. Hansen, T. Vegge, DFT + *U* study of strain-engineered CO_2 reduction on a CeO_{2-x} (111) facet, J. Phys. Chem. C 125 (2021) 14221–14227.
[139] N. Kumari, M.A. Haider, M. Agarwal, N. Sinha, S. Basu, Role of reduced CeO_2 (110) surface for CO_2 reduction to CO and methanol, J. Phys. Chem. C 120 (2016) 16626–16635.
[140] Y. Yu, et al., CO_2 activation and carbonate intermediates: an operando AP-XPS study of CO_2 electrolysis reactions on solid oxide electrochemical cells, Phys. Chem. Chem. Phys. 16 (2014) 11633–11639.
[141] J. Wang, et al., Threshold catalytic onset of carbon formation on CeO_2 during CO_2 electrolysis: mechanism and inhibition, J. Mater. Chem. A 7 (2019) 15233–15243.
[142] T. Staudt, et al., Electronic structure of magnesia−ceria model catalysts, CO_2 adsorption, and CO_2 activation: a synchrotron radiation photoelectron spectroscopy study, J. Phys. Chem. C 115 (2011) 8716–8724.
[143] M. Bugnet, S.H. Overbury, Z.L. Wu, T. Epicier, Direct visualization and control of atomic mobility at {100} surfaces of ceria in the environmental transmission electron microscope, Nano Lett. 17 (2017) 7652–7658.
[144] A. Bruix, K.M. Neyman, How to design models for ceria nanoparticles: challenges and strategies for describing nanostructured reducible oxides, Front. Nanosci. 12 (2018) 55–99. Elsevier.
[145] A. Trovarelli, J. Llorca, Ceria catalysts at nanoscale: how do crystal shapes shape catalysis? ACS Catal. 7 (2017) 4716–4735.
[146] E. Aneggi, M. Boaro, S. Colussi, C. de Leitenburg, A. Trovarelli, Ceria-Based materials in catalysis, in: Handbook on the Physics and Chemistry of Rare Earths vol. 50, Elsevier, 2016, pp. 209–242.
[147] Z. Wu, M. Li, S.H. Overbury, On the structure dependence of CO oxidation over CeO2 nanocrystals with well-defined surface planes, J. Catal. 285 (2012) 61–73.
[148] Y. Cao, et al., Getting insights into the influence of crystal plane effect of shaped ceria on its catalytic performances, J. Phys. Chem. C 122 (2018) 20402–20409.
[149] S. Wang, et al., Morphology control of ceria nanocrystals for catalytic conversion of CO2 with methanol, Nanoscale 5 (2013) 5582.
[150] Z. Wu, M. Li, D.R. Mullins, S.H. Overbury, Probing the surface sites of CeO_2 nanocrystals with well-defined surface planes via methanol adsorption and desorption, ACS Catal. 2 (2012) 2224–2234.
[151] A.K.P. Mann, Z. Wu, F.C. Calaza, S.H. Overbury, Adsorption and reaction of acetaldehyde on shape-controlled CeO_2 nanocrystals: elucidation of structure–function relationships, ACS Catal. 4 (2014) 2437–2448.
[152] H. Huang, Q. Dai, X. Wang, Morphology effect of Ru/CeO2 catalysts for the catalytic combustion of chlorobenzene, Appl. Catal. B Environ. 158–159 (2014) 96–105.
[153] K. Zhou, X. Wang, X. Sun, Q. Peng, Y. Li, Enhanced catalytic activity of ceria nanorods from well-defined reactive crystal planes, J. Catal. 229 (2005) 206–212.
[154] Q. Dai, et al., Catalysis oxidation of 1,2-dichloroethane and ethyl acetate over ceria nanocrystals with well-defined crystal planes, Appl. Catal. B Environ. 117–118 (2012) 360–368.
[155] L. Torrente-Murciano, et al., Shape-dependency activity of nanostructured CeO2 in the total oxidation of polycyclic aromatic hydrocarbons, Appl. Catal. B Environ. 132–133 (2013) 116–122.
[156] H.-X. Mai, et al., Shape-selective synthesis and oxygen storage behavior of ceria nanopolyhedra, nanorods, and nanocubes, J. Phys. Chem. B 109 (2005) 24380–24385.
[157] Y. Li, et al., Effects of CeO2 support facets on VOx/CeO2 catalysts in oxidative dehydrogenation of methanol, J. Catal. 315 (2014) 15–24.
[158] M. Lykaki, E. Pachatouridou, E. Iliopoulou, S.A.C. Carabineiro, M. Konsolakis, Impact of the synthesis parameters on the solid state properties and the CO oxidation performance of ceria nanoparticles, RSC Adv. 7 (2017) 6160–6169.
[159] Z. Wu, M. Li, J. Howe, H.M. Meyer, S.H. Overbury, Probing defect sites on CeO_2 nanocrystals with well-defined surface planes by raman spectroscopy and O_2 adsorption, Langmuir 26 (2010) 16595–16606.
[160] S. Agarwal, et al., Exposed surfaces on shape-controlled ceria nanoparticles revealed through AC-TEM and water-gas shift reactivity, ChemSusChem 6 (2013) 1898–1906.
[161] C. Yang, et al., Surface faceting and reconstruction of ceria nanoparticles, Angew. Chem. Int. Ed. 56 (2017) 375–379.
[162] J. Zhang, X.-Q. Gong, G. Lu, Catalytic activities of CeO_2(110)–2 × 1 reconstructed surface, Surf. Sci. 632 (2015) 164–173.
[163] P.A. Crozier, R. Wang, R. Sharma, In situ environmental TEM studies of dynamic changes in cerium-based oxides nanoparticles during redox processes, Ultramicroscopy 108 (2008) 1432–1440.
[164] F. Polo-Garzon, Z. Bao, X. Zhang, W. Huang, Z. Wu, Surface reconstructions of metal oxides and the consequences on catalytic chemistry, ACS Catal. 9 (2019) 5692–5707.
[165] X. Liu, K. Zhou, L. Wang, B. Wang, Y. Li, Oxygen vacancy clusters promoting reducibility and activity of ceria nanorods, J. Am. Chem. Soc. 131 (2009) 3140–3141.
[166] T. Désaunay, et al., Surface-dependent oxidation of H_2 on CeO_2 surfaces, J. Catal. 297 (2013) 193–201.
[167] H. Li, et al., Morphological impact of manganese–cerium oxides on ethanol oxidation, Catal. Sci. Technol. 1 (2011) 1677.
[168] M. Kovacevic, B.L. Mojet, J.G. van Ommen, L. Lefferts, Effects of morphology of cerium oxide catalysts for reverse water gas shift reaction, Catal. Lett. 146 (2016) 770–777.
[169] T. Wu, N. López, T. Vegge, H.A. Hansen, Facet-dependent electrocatalytic water splitting reaction on CeO_2: A DFT + U study, J. Catal. 388 (2020) 1–10.
[170] X. Tong, et al., Shape-dependent activity of ceria for hydrogen electro-oxidation in reduced-temperature solid oxide fuel cells, Small 11 (2015) 5581–5588.
[171] R. Sinclair, S.C. Lee, Y. Shi, W.C. Chueh, Structure and chemistry of epitaxial ceria thin films on yttria-stabilized zirconia substrates, studied by high resolution electron microscopy, Ultramicroscopy 176 (2017) 200–211.
[172] G. Vilé, S. Colussi, F. Krumeich, A. Trovarelli, J. Pérez-Ramírez, Opposite face sensitivity of CeO_2 in hydrogenation and oxidation catalysis, Angew. Chem. Int. Ed. 53 (2014) 12069–12072.
[173] S. Grieshammer, B.O.H. Grope, J. Koettgen, M. Martin, A combined DFT + U and Monte Carlo study on rare earth doped ceria, Phys. Chem. Chem. Phys. 16 (2014) 9974.
[174] J. Faber, C. Geoffroy, A. Roux, A. Sylvestre, P. Abélard, A Systematic investigation of the dc electrical conductivity of rare-earth doped ceria, Appl. Phys. Solids Surf. 49 (1989) 225–232.
[175] D. Wang, D. Park, J. Griffith, A. Nowick, Oxygen-ion conductivity and defect interactions in yttria-doped ceria, Solid State Ionics 2 (1981) 95–105.
[176] M.D. Krcha, A.D. Mayernick, M.J. Janik, Periodic trends of oxygen vacancy formation and C–H bond activation over transition metal-doped CeO2 (111) surfaces, J. Catal. 293 (2012) 103–115.
[177] M. Nolan, Molecular adsorption on the doped (110) ceria surface, J. Phys. Chem. C 113 (2009) 2425–2432.
[178] A.D. Mayernick, M.J. Janik, Methane activation and oxygen vacancy formation over CeO_2 and Zr, Pd substituted CeO_2 surfaces, J. Phys. Chem. C 112 (2008) 14955–14964.
[179] A. Fuerte, R. Ximena Valenzuela, M. José Escudero, Role of dopants on ceria-based anodes for it-sofcs powered by hydrocarbon fuels, Univers. J. Electr. Electron. Eng. 5 (2017) 45–55.
[180] Z. Yang, G. Luo, Z. Lu, T.K. Woo, K. Hermansson, Structural and electronic properties of NM-doped ceria (NM = Pt, Rh): a first-principles study, J. Phys. Condens. Matter 20 (2008), 035210.
[181] K.R. Priolkar, et al., Formation of $Ce_{1-x}Pd_xO_{2-\delta}$ solid solution in combustion-synthesized Pd/CeO_2 catalyst: XRD, XPS, and EXAFS investigation, Chem. Mater. 14 (2002) 2120–2128.
[182] R. Jacot, R. Moré, R. Michalsky, A. Steinfeld, G.R. Patzke, Trends in the phase stability and thermochemical oxygen exchange of ceria doped with potentially tetravalent metals, J. Mater. Chem. A 5 (2017) 19901–19913.
[183] A. Hornés, et al., Structural, catalytic/redox and electrical characterization of systems combining Cu–Fe with CeO2 or Ce1−xMxO2−δ (M=Gd or Tb) for direct methane oxidation, J. Power Sources 196 (2011) 4218–4225.
[184] T. Wu, Q. Deng, H.A. Hansen, T. Vegge, Mechanism of water splitting on gadolinium-doped CeO_2 (111): A DFT + *U* study, J. Phys. Chem. C 123 (2019) 5507–5517.
[185] J.J. Carey, M. Nolan, Cation doping size effect for methane activation on alkaline earth metal doping of the CeO_2 (111) surface, Catal. Sci. Technol. 6 (2016) 3544–3558.
[186] M. Nolan, Enhanced oxygen vacancy formation in ceria (111) and (110) surfaces doped with divalent cations, J. Mater. Chem. 21 (2011) 9160.
[187] V. Shapovalov, H. Metiu, Catalysis by doped oxides: CO oxidation by AuxCe1−xO2, J. Catal. 245 (2007) 205–214.
[188] M. Nolan, V.S. Verdugo, H. Metiu, Vacancy formation and CO adsorption on gold-doped ceria surfaces, Surf. Sci. 602 (2008) 2734–2742.
[189] W. Tang, et al., Methane complete and partial oxidation catalyzed by Pt-doped CeO2, J. Catal. 273 (2010) 125–137.
[190] J. Wang, X.-Q. Gong, A DFT + U study of V, Cr and Mn doped CeO2(111), Appl. Surf. Sci. 428 (2018) 377–384.
[191] C. Kang, H. Kusaba, H. Yahiro, K. Sasaki, Y. Teraoka, Preparation, characterization and electrical property of Mn-doped ceria-based oxides, Solid State Ionics 177 (2006) 1799–1802.
[192] M. Nolan, Formation of Ce3+ at the cerium dioxide (110) surface by doping, Chem. Phys. Lett. 492 (2010) 115–118.
[193] C. Chatzichristodoulou, et al., Enhanced reducibility and electronic conductivity of Nb or W doped Ce0.9Gd0.1O1.95−δ, Solid State Ionics 269 (2015) 51–56.
[194] K. Sudarshan, V. Tiwari, P. Utpalla, S.K. Gupta, Defect evolution in Eu^{3+}, Nb^{5+} doped and co-doped CeO_2: X-ray diffraction, positron annihilation lifetime and photoluminescence studies, Inorg. Chem. Front. 6 (2019) 2167–2177.
[195] C. Muhich, M. Hoes, A. Steinfeld, Mimicking tetravalent dopant behavior using paired charge compensating dopants to improve the redox performance of ceria for thermochemically splitting H2O and CO2, Acta Mater. 144 (2018) 728–737.
[196] Christodoulos Chatzichristodoulou, Peter Vang Hendriksen, Anke Hagen, Defect chemistry and thermomechanical properties of Ce0.8PrxTb0.2-xO2-δ, J. Electrochem. Soc. 157 (2) (2010) B299–B307.

[197] A.A. AlKhoori, et al., Cu, Sm co-doping effect on the CO oxidation activity of CeO2. A combined experimental and density functional study, Appl. Surf. Sci. 521 (2020), 146305.

[198] Z. Zhao, M. Uddi, N. Tsvetkov, B. Yildiz, A.F. Ghoniem, Redox kinetics and nonstoichiometry of $Ce_{0.5}$ $Zr_{0.5}$ $O_{2-\delta}$ for water splitting and hydrogen production, J. Phys. Chem. C 121 (2017) 11055–11068.

[199] W. Yuan, et al., Unexpected trends in the enhanced Ce^{3+} surface concentration in ceria–zirconia catalyst materials, J. Mater. Chem. A 8 (2020) 9850–9858.

[200] C. Graves, C. Chatzichristodoulou, M.B. Mogensen, Kinetics of CO/CO $_2$ and H_2/H_2 O reactions at Ni-based and ceria-based solid-oxide-cell electrodes, Faraday Discuss. 182 (2015) 75–95.

[201] Y. Wang, Y. Wang, C. Xia, Surface process of doped ceria reduction by electrical conductivity relaxation, J. Electrochem. Soc. 159 (2012) F570–F576.

[202] N. Yang, et al., Effects of dopant ionic radius on cerium reduction in epitaxial cerium oxide thin films, J. Phys. Chem. C 121 (2017) 8841–8849.

[203] S. Li, et al., Europium-doped ceria nanowires as anode for solid oxide fuel cells, Front. Chem. 8 (2020) 348.

[204] N. Kumari, M.A. Haider, P.K. Tiwari, S. Basu, Carbon dioxide reduction on the composite of copper and praseodymium-doped ceria electrode in a solid oxide electrolysis cells, Ionics 25 (2019) 3165–3177.

[205] X. Zhang, et al., Enhancing electrocatalytic CO2 reduction in solid oxide electrolysis cell with Ce0.9Mn0.1O2−δ nanoparticles-modified LSCM-GDC cathode, J. Catal. 359 (2018) 8–16.

[206] Zhidong Huang, et al., Charge transfer reactions in CO2 electroreduction on manganese doped ceria, ChemElectroChem 6 (2019) 5.

[207] Z. Huang, et al., Enhancing cathode performance for CO2 electrolysis with Ce0.9M0.1O2− (M=Fe, Co, Ni) catalysts in solid oxide electrolysis cell, J. Energy Chem. 40 (2020) 46–51.

[208] W. Wang, et al., Enhanced carbon dioxide electrolysis at redox manipulated interfaces, Nat. Commun. 10 (2019) 1550.

[209] S. Lee, M. Kim, K.T. Lee, J.T.S. Irvine, T.H. Shin, Enhancing electrochemical CO_2 reduction using Ce(Mn,Fe)O $_2$ with La(Sr)Cr(Mn)O_3 cathode for high-temperature solid oxide electrolysis cells, Adv. Energy Mater. 11 (2021), 2100339.

[210] G.F. Harrington, et al., The interplay and impact of strain and defect association on the conductivity of rare-earth substituted ceria, Acta Mater. 166 (2019) 447–458.

[211] K. Wen, W. Lv, W. He, Interfacial lattice-strain effects on improving the overall performance of micro-solid oxide fuel cells, J. Mater. Chem. A 3 (2015) 20031–20050.

[212] B. Yildiz, "Stretching" the energy landscape of oxides—Effects on electrocatalysis and diffusion, MRS Bull. 39 (2014) 147–156.

[213] R.A. De Souza, A. Ramadan, S. Hörner, Modifying the barriers for oxygen-vacancy migration in fluorite-structured CeO $_2$ electrolytes through strain: a computer simulation study, Energy Environ. Sci. 5 (2012) 5445–5453.

[214] M.J.D. Rushton, A. Chroneos, Impact of uniaxial strain and doping on oxygen diffusion in CeO2, Sci. Rep. 4 (2015) 6068.

[215] L. Sun, D. Marrocchelli, B. Yildiz, Edge dislocation slows down oxide ion diffusion in doped CeO2 by segregation of charged defects, Nat. Commun. 6 (2015) 6294.

[216] D. Pergolesi, et al., Tensile lattice distortion does not affect oxygen transport in yttria-stabilized zirconia–CeO_2 heterointerfaces, ACS Nano 6 (2012) 10524–10534.

[217] N.H. Perry, G.F. Harrington, H.L. Tuller, Electrochemical ionic interfaces, Metal Oxide-Based Thin Film Struct. (2018) 79–106. Elsevier, https://doi.org/10.1016/B978-0-12-811166-6.00004-2.

[218] R.P. Jansonius, L.M. Reid, C.N. Virca, C.P. Berlinguette, Strain engineering electrocatalysts for selective CO_2 reduction, ACS Energy Lett. 4 (2019) 980–986.

[219] B. You, et al., Enhancing electrocatalytic water splitting by strain engineering, Adv. Mater. 31 (2019) 1807001.

[220] J.D. Nicholas, Y. Qi, S.R. Bishop, P.P. Mukherjee, Introduction to mechano-electro-chemical coupling in energy related materials and devices, J. Electrochem. Soc. 161 (2014) Y11–Y12.

[221] A. Kushima, S. Yip, B. Yildiz, Competing strain effects in reactivity of $LaCoO_3$ with oxygen, Phys. Rev. B 82 (2010), 115435.

[222] H. Jalili, J.W. Han, Y. Kuru, Z. Cai, B. Yildiz, New insights into the strain coupling to surface chemistry, electronic structure, and reactivity of $La_{0.7}$ $Sr_{0.3}$ MnO_3, J. Phys. Chem. Lett. 2 (2011) 801–807.

[223] Z. Cai, Y. Kuru, J.W. Han, Y. Chen, B. Yildiz, Surface electronic structure transitions at high temperature on perovskite oxides: the case of strained $La_{0.8}$ $Sr_{0.2}$ CoO_3 thin films, J. Am. Chem. Soc. 133 (2011) 17696–17704.

[224] M. Kubicek, et al., tensile lattice strain accelerates oxygen surface exchange and diffusion in La_{1-x} Sr_x $CoO_{3-\delta}$ thin films, ACS Nano 7 (2013) 3276–3286.

[225] C. Balaji Gopal, et al., Equilibrium oxygen storage capacity of ultrathin CeO2-δ depends non-monotonically on large biaxial strain, Nat. Commun. 8 (2017) 15360.

[226] K. Ahn, et al., Lattice-strain effect on oxygen vacancy formation in gadolinium-doped ceria, J. Electroceram. 32 (2014) 72–77.

[227] D. Ma, et al., Effect of lattice strain on the oxygen vacancy formation and hydrogen adsorption at CeO2(111) surface, Phys. Lett. A 378 (2014) 2570–2575.

[228] Z.-K. Han, L. Zhang, M. Liu, M.V. Ganduglia-Pirovano, Y. Gao, The structure of oxygen vacancies in the near-surface of reduced CeO2 (111) under strain, Front. Chem. 7 (2019) 436.

[229] M.V. Ganduglia-Pirovano, J.L.F. Da Silva, J. Sauer, Density-functional calculations of the structure of near-surface oxygen vacancies and electron localization on CeO_2 (111), Phys. Rev. Lett. 102 (2009), 026101.

[230] T.X.T. Sayle, et al., Strain and architecture-tuned reactivity in ceria nanostructures; enhanced catalytic oxidation of CO to CO_2, Chem. Mater. 24 (2012) 1811–1821.

[231] T. Wu, T. Vegge, H.A. Hansen, Improved electrocatalytic water splitting reaction on CeO_2 (111) by strain engineering: a DFT+ *U* study, ACS Catal. 9 (2019) 4853–4861.

[232] Y. Shi, et al., Growth of highly strained CeO_2 ultrathin films, ACS Nano 10 (2016) 9938–9947.

[233] P.V. Hendriksen, et al., Failure modes of thin supported membranes, Adv. Solid Oxide Fuel Cells 15 (2007).

[234] A. Kaiser, et al., Evaluation of thin film ceria membranes for syngas membrane reactors—Preparation, characterization and testing, J. Membr. Sci. 378 (2011) 51–60.

[235] H. Han, et al., Lattice strain-enhanced exsolution of nanoparticles in thin films, Nat. Commun. 10 (2019) 1471.

[236] F. Baiutti, et al., A high-entropy manganite in an ordered nanocomposite for long-term application in solid oxide cells, Nat. Commun. 12 (2021) 2660.

[237] M.P. Wells, et al., Route to high-performance micro-solid oxide fuel cells on metallic substrates, ACS Appl. Mater. Interfaces 13 (2021) 4117–4125.

[238] P. Strasser, et al., Lattice-strain control of the activity in dealloyed core–shell fuel cell catalysts, Nat. Chem. 2 (2010) 454–460.

[239] T. Ellaby, et al., Strain effects in core–shell PtCo nanoparticles: a comparison of experimental observations and computational modelling, Phys. Chem. Chem. Phys. 22 (2020) 24784–24795.

[240] J.T.L. Gamler, et al., Effect of lattice mismatch and shell thickness on strain in core@shell nanocrystals, Nanoscale Adv. 2 (2020) 1105–1114.

[241] A. Bhargava, et al., Enhanced Li-ion diffusion and electrochemical performance in strained-manganese–iron oxide core–shell nanoparticles, J. Chem. Phys. 155 (2021), 144702.

[242] P. Boldrin, et al., Strategies for carbon and sulfur tolerant solid oxide fuel cell materials, incorporating lessons from heterogeneous catalysis, Chem. Rev. 116 (2016) 13633–13684.

[243] W. Zhu, C. Xia, J. Fan, R. Peng, G. Meng, Ceria coated Ni as anodes for direct utilization of methane in low-temperature solid oxide fuel cells, J. Power Sources 160 (2006) 897–902.

[244] M.M. Welander, et al., What does carbon tolerant really mean? *Operando* vibrational studies of carbon accumulation on novel solid oxide fuel cell anodes prepared by infiltration, Phys. Chem. Chem. Phys. 22 (2020) 9815–9823.

[245] Y. Yu, et al., Carbon deposits and PT/YSZ overpotentials In CO/CO2 Solid oxide electrochemical cells, ECS Trans. 57 (2013) 3119–3126.

[246] X. Li, et al., Large-area synthesis of high-quality and uniform graphene films on copper foils, Science 324 (2009) 1312–1314.

[247] T.L. Skafte, P. Blennow, J. Hjelm, C. Graves, Carbon deposition and sulfur poisoning during CO2 electrolysis in nickel-based solid oxide cell electrodes, J. Power Sources 373 (2018) 54–60.

[248] J.T.S. Irvine, et al., Evolution of the electrochemical interface in high-temperature fuel cells and electrolysers, Nat. Energy 1 (2016) 15014.

[249] J. Myung, D. Neagu, D.N. Miller, J.T.S. Irvine, Switching on electrocatalytic activity in solid oxide cells, Nature 537 (2016) 528–531.

[250] K. Kooser, et al., Operando high-temperature near-ambient pressure X-ray photoelectron spectroscopy and impedance spectroscopy study of Ni − $Ce_{0.9}$ $Gd_{0.1}$ O_2 − δ solid oxide fuel cell anode, Int. J. Hydrog. Energy 45 (2020) 25286–25298.

[251] X. Garcia, et al., Ceria-based catalysts studied by near ambient pressure X-ray photoelectron spectroscopy: a review, Catalysts 10 (2020) 286.

[252] C. Zhang, et al., Multielement activity mapping and potential mapping in solid oxide electrochemical cells through the use of *operando* XPS, ACS Catal. 2 (2012) 2297–2304.

[253] L. Trotochaud, A.R. Head, O. Karslıoğlu, L. Kyhl, H. Bluhm, Ambient pressure photoelectron spectroscopy: practical considerations and experimental frontiers, J. Phys. Condens. Matter 29 (2017), 053002.

[254] Y. Han, H. Zhang, Y. Yu, Z. Liu, In situ characterization of catalysis and electrocatalysis using APXPS, ACS Catal. 11 (2021) 1464–1484.

[255] A. Stangl, D. Muñoz-Rojas, M. Burriel, In situ and Operando Characterisation Techniques for Solid Oxide Electrochemical Cells: Recent Advances. 13, 2021.